

An Omics Approach to Mixed-Anion Electrolyte Discovery for Lithium Metal Batteries for Electric Aircraft

Youngmin Ko,¹ Michael A. Baird,² Xinxing Peng,³ Tofunmi Ogunfunmi,⁴ Young-Woon Byeon,⁵ Liana M. Klivansky,¹ Haegyeom Kim,⁵ Mary C. Scott,^{3,4} Brett A. Helms^{1,5}*

¹The Molecular Foundry, Lawrence Berkeley National Laboratory, Berkeley, California, 94720, United States

²Department of Chemistry, University of California, Berkeley, California, 94720, United States

³National Center for Electron Microscopy, Lawrence Berkeley National Laboratory, Berkeley, California, 94720, United States

⁴Department of Materials Science and Engineering, University of California, Berkeley, California, 94720, United States

⁵Materials Sciences Division, Lawrence Berkeley National Laboratory, Berkeley, California, 94720, United States

*Corresponding author (B. A. Helms): bahelms@lbl.gov

Abstract

Battery systems for electric aircraft ideally feature high energy density electrode materials configured in cell architectures that deliver high power on demand. Full cathode utilization requires electrolytes that permit charging to high voltage, during which conventional electrolytes undergo decomposition. If the associated rise in impedance is uncontrolled, then discharging at high current density for power is unsustainable. It remains a challenge to design electrolytes from the perspective of battery interphases to control these phenomena. Here, we advance an omics approach to understand how lithium salts in locally super-concentrated electrolytes (LSCEs) should be mixed to create stable ionically conductive interphases in high-power Li|NMC811 cells charged to high voltage. Mixed-anion LCSEs maintain an areal ion flux of 6 mA cm^{-2} during discharge across 500 cycles with 70% capacity retention, outperforming single-salt LSCEs as well as single- and dual-salt concentrated electrolytes. These advantages stem from the enrichment of cathode-electrolyte interphases with fluoroethers, which suppress cathode corrosion and fracturing. Cell chemistry, architecture, and mission must be considered together when designing electrolytes for emerging segments in electric mobility and omics provides a vantage point for tying battery performance to chemical complexity in battery interphases.

Introduction

Electric aircraft for urban mobility require batteries with high energy density for cargo and range as well as high power for take-off and landing.¹⁻³ Lithium metal batteries featuring nickel-rich layered oxide cathodes (e.g., $\text{LiNi}_{0.8}\text{Mn}_{0.1}\text{Co}_{0.1}\text{O}_2$, or NMC811) are well positioned to satisfy these demands, however, accessing the full capacity of the cathode has been limited with dilute, concentrated, and locally super-concentrated electrolytes (LSCEs) due to electrode and electrolyte degradation at high potential. The impedance rise in Li|NMC811 cells associated with these degradation phenomena remain problematic for delivering power reliably over time, particularly at low states-of-charge when the aircraft attempts to land.⁴⁻⁶ Needed are electrolytes that form self-limiting ionically-conducting interphases with both electrodes such that the leakage current is minimized on charge at high voltage,

the structural integrity of cathode particles is managed, and the impedance rise over time is low to ensure cells do not become power-compromised during their missions.

Here, we advance an omics approach to accelerate the discovery and understanding of electrolytes and interphases for batteries designed for electric aircraft. Omics is routinely used to study collective changes across genomes, proteomes, and metabolomes in biological systems comprising their response to perturbation from their native state.^{7, 8} An omics approach to battery electrolytes and interphases recognizes that even the most subtle changes to electrolyte composition trigger non-trivial changes to interphasial chemistries that may be revealed through quantitative structural characterization. However, a detailed understanding of degradation and failure is ultimately needed to link interphase structure, function, and evolution to battery performance. Taking this omics approach, we explored a mixed-anion strategy for creating LSCEs that generate stable interphases on both lithium metal and NMC811 up to 4.35 V vs. Li/Li⁺, while supporting an areal ion flux of 6 mA cm⁻² in Li|NMC811 cells relevant to electric aircraft (**Figure 1a** and **1b**). By adding either LiClO₄ or lithium difluorooxalatoborate (LiDFOB) to LSCEs comprising lithium *bis*(fluorosulfonyl)imide (LiFSI), 1,2-dimethoxyethane (DME), and 1,1,2,2-tetrafluoroethyl-2,2,3,3-tetrafluoropropyl ether (TTE), we suppress the leakage current tied to both electrochemical and chemical reactions at electrolyte–NMC interfaces. Li|NMC811 cells implementing mixed-anion LSCEs exhibit a shallow rise in cell impedance and retain 70% of their initial capacity after 500 cycles under continuous high-power operation, outperforming single-salt LSCEs (e.g., 70% capacity retention at cycle 370) as well as single- and dual-salt concentrated electrolytes. We exploited these advantages in anodeless cells, where LiClO₄ stood out as the superior additive for its ability to lower the lithium consumption rate. Postmortem analysis of Li|NMC811 cells revealed that the failure mechanism typified by a single-anion approach is cathode degradation and fracturing, which is resolved with the mixed-anion approach. However, in high-power anodeless cells, where the confluence of cathode degradation and lithium inventory management is limiting, specific mixtures of anions are needed to extend cycle life: e.g., 50% capacity retention after 100 cycles with LiClO₄ added alongside LiFSI in the LSCEs compared to only 5% retention after 50 cycles with LiDFOB added and 13% retention after 100 cycles with LiFSI alone. Using omics, we identified

specific “up-regulated” and “down-regulated” components of the interphase providing enhanced performance and stability. These changes were accounted for by changes in DME activity, which is broadly tunable in the mixed-anion LSCE paradigm.

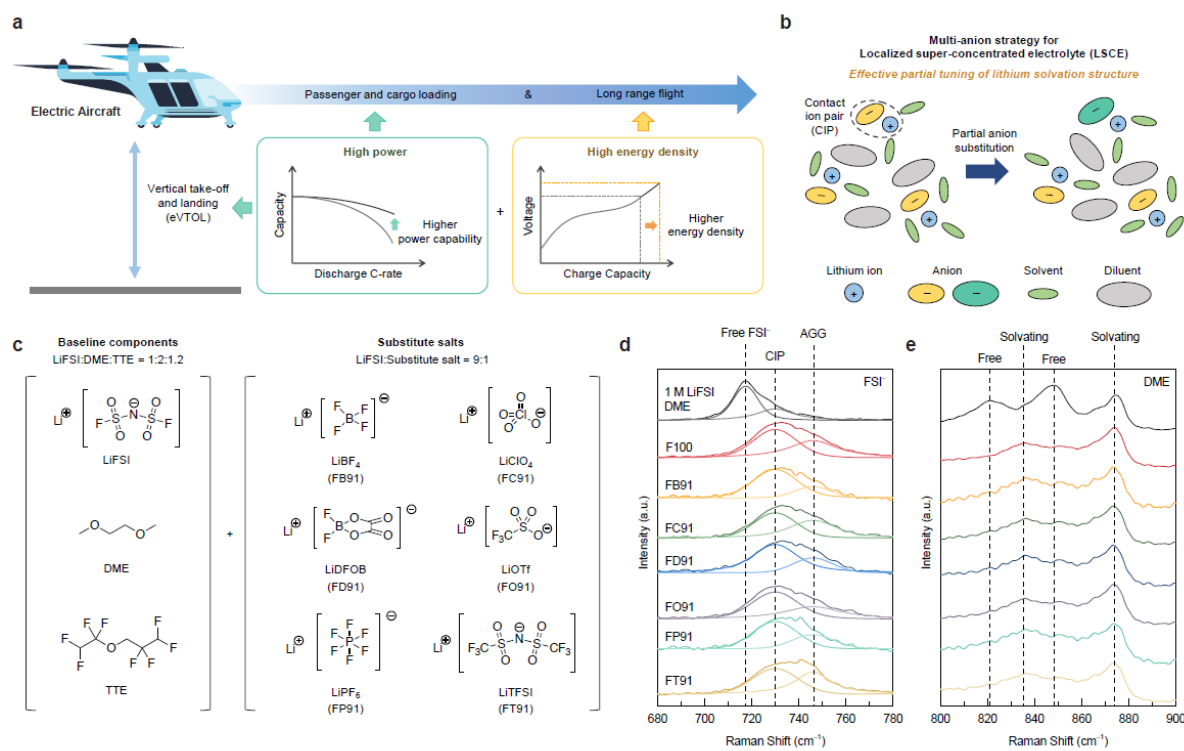


Figure 1. Mixed-anion LSCEs for high-power and high-voltage batteries for electric aircraft. a, Electric aircraft requiring high power and high energy density battery systems for take-off, landing, passenger and cargo loading, and long-range flight. **b**, Mixed-anion strategy to modulate CIPs in LSCEs. **c**, Electrolyte components and their ratio in the LSCEs considered. **d–e**, Raman spectra showing vibration mode of FSI⁻ anion (**d**), and DME in LSCEs (**e**).

As deep decarbonization of transportation begins to take shape through electrification, it is increasingly recognized that batteries intended for different sectors may not be transferrable between them.^{1, 9, 10} It follows that electrolytes for similar battery chemistries may not be transferrable, as the failure mechanisms for those cells will depend both on the cell architectures and power requirements across the life cycle of the battery system. We show that for high-power applications, a mixed-anion approach

addresses the most critical problems underlying cell failure in high energy density cells, with or without an explicit lithium metal anode. This knowledge builds on and complements related work in concentrated electrolytes and LSCEs intended for EVs, where the power requirements are not as demanding.¹¹⁻¹⁴ In particular, a growing number of salts, solvents, diluents, and additives have been developed for advanced electrolytes with considerable promise.^{4, 13, 15-25} We anticipate that these and others could be put to work in future iterations of mixed-anion LSCEs to fine-tune electrolyte performance in batteries for electric vehicles, aircraft, and seacraft. We further see as opportune recent advances in robotics and machine learning-guided autonomous electrolyte discovery to accelerate the identification of relevant combinations for those applications using omics to close the loop.²⁶⁻²⁸

Exploration of chemical space in mixed-anion LSCEs

Anion redox is a contributor to interphase generation in batteries.^{29, 30} Combining lithium salts with different anions introduces the possibility of creating hybrid interphases that would not form otherwise.^{11, 31} The interplay of (mixed) anion and solvent redox in interphase generation will depend on speciation of lithium salts in the electrolyte, which is dictated by salt concentration as well as the influence of electric fields at battery interfaces.^{13, 32, 33} Likewise, when using mixtures of coordinating and non-coordinating solvents, those that produce contact ion pairs (CIP) and aggregates (AGG) of ions and solvent significantly alter anion and solvent activity at electrified interfaces; LSCEs are exemplars of this behavior.^{14, 30} We lack an understanding for how to combine anions in clustered electrolytes to guide interphase generation, particularly in batteries whose missions vary widely across different applications.

Here, we considered these aspects in LSCEs for batteries with high energy density and power relevant to electric aircraft. Our LSCEs featured LiFSI in combination with either LiBF₄ (FB91), LiClO₄ (FC91), lithium difluoro(oxalate)borate (LiDFOB) (FD91), LiOTf (FO91), LiPF₆ (FP91), or LiTFSI (FT91) in a molar ratio of LiFSI:Salt:DME:TTE of 0.9 : 0.1 : 2 : 1.2 (**Figure 1c**). We confirmed by Raman spectroscopy that mixing anions in LSCEs generated CIPs containing FSI⁻ at 730 cm⁻¹ along with AGGs

of ions and solvent at 746 cm^{-1} with some variation in relative proportion; these were distinct from free FSI^- , which had a characteristic band at 717 cm^{-1} in dilute electrolyte formulations (**Figure 1d–e** and **Supplementary Figure 1**). In the cases of FC91 and FT91, the prevalence of AGGs is slightly elevated over CIPs relative to what is observed for other LSCEs. We also found little evidence for “free” DME in the LSCEs, where bands at 836 cm^{-1} and 874 cm^{-1} indicate bonding between DME and lithium ions; in dilute electrolytes, free DME is characterized by bands at 821 cm^{-1} and 848 cm^{-1} .

Free DME limits electrolyte stability at high voltage; reducing DME activity, through coordination to Li^+ , enhances electrolyte stability in concentrated electrolytes and LSCEs.^{11, 32} We confirmed this in linear sweep voltammetry (LSV) in $\text{Li}|\text{Al}$ cells for a dilute electrolyte featuring LiFSI and DME as well as in an LSCE formulated with LiFSI alone (**Supplementary Figure 2a–b**). With regard to the former, the earliest onset of current tied to electrolyte oxidation preceded 3.0 V vs. Li/Li^+ and was followed by a steep rise above 4.5 V . With regard to the latter, the onset remained essentially unchanged, but the steep rise was suppressed from 4.5 V to $>5.75\text{ V}$. In contrast, we found that the mixed-anion approach to LSCEs increased the onset potential for electrolyte degradation, in select cases up to 3.75 V . These increases, suggesting improvements in stability, are listed in the following order: $\text{LiClO}_4 < \text{LiOTf} = \text{LiTFSI} < \text{LiPF}_6 < \text{LiDFOB} < \text{LiBF}_4$. Based on these data, we chose to further assess the advantages of the mixed-anion approach to LSCEs in $\text{Li}|\text{NMC811}$ cells charged to a potential up to 4.35 V , which places the additives on an equal footing, considering their bulk transport properties are similar (**Supplementary Figure 2c**). This allows us to differentiate their behavior essentially on the basis of interphase generation and degradation.

Compatibility of mixed-anion LSCEs with high-nickel NMC cathodes

We assessed the compatibility of LSCEs against NMC811 by several strategies, aiming to understand cathode-specific interactions as well as the implications of anode–cathode crosstalk during electrolyte degradation at high voltage over time. We initially monitored the leakage current density in $\text{Li}|\text{NMC811}$ cells over 12 h on the first charge, where we held the voltage at 4.35 V after charging the cell at low

current density (C/15). These experiments evaluated the initial rates of electrolyte decomposition during formation. All approach steady-state after ~2 h. Mixed-anion LSCEs containing LiClO₄ and LiDFOB—FC91 and FD91, respectively—showed lower leakage current densities at steady-state compared to the LSCE containing LiFSI alone (F100); on the other hand, the remaining mixed-anion LSCEs showed higher leakage current densities (**Figure 2a**). These trends were consistent with similar experiments conducted at a constant voltage hold of 4.2 V (**Supplementary Figure 3**). We then determined the leakage current capacity to quantify the extent of electrolyte degradation at the prescribed potential during formation (**Figure 2b**); we integrated the leakage current density between 2 and 12 h (i.e., at steady-state) to minimize the apparent contribution from the Faradaic current tied to NMC charging. We found that LSCEs FC91 and FD91 exclusively decreased the extent of electrolyte degradation, by up to 44%, compared to the LSCE with LiFSI alone.

To understand the integrity of this interphase, we extracted the cathodes of Li|NMC811 cells charged at constant current density of 0.3 mA cm⁻² to 4.35 V and held there for 1 h, allowing the current to decrease over time. We then assembled NMC811|NMC811 cells with the extracted cathodes alongside pristine cathodes. Both cathodes have identical composition, and notably, only the extracted cathodes feature an interphase. We then moved charge between the electrodes at 1 mA cm⁻², monitoring the retained capacity over 100 cycles (**Figure 2c–d**). In these experiments, the energy stored in the original cathodes extracted from the Li|NMC811 cells dictates the chemical potential in the system available for directing further reactions at electrolyte–electrode interfaces, along with the electrochemical driving force needed to maintain the current density. Cathodes oxidized to higher potential, once integrated in NMC811|NMC811 cells, will have stronger driving forces for electrolyte degradation at the pristine cathodes than those with lower stored energy. If interphase generation were not fast and self-limiting, then extracted cathodes with the most stored charge would lose their stored charge to electrolyte degradation at the surface of the pristine cathode.

Cathodes extracted from Li|NMC811 cells featuring FD91 retained more of their stored charge (~1.1 mAh cm⁻²) than the others (0.7–1.0 mAh cm⁻²) (**Supplementary Figure 4**). Even so,

NMC811|NMC811 cells implementing FD91 sustainably cycled in the rocking-chair cell. Symmetric cells implementing FC91 were likewise stable, whereas all others showed continuous loss of the lithium inventory. This suggested that mixed-anion LSCEs featuring LiFSI alongside LiClO₄ or LiDFOB quickly form an ionically conductive, yet electronically passivating interphases on NMC811 particles in cathodes charged to high potential.

Subsequent to formation, it is important for the interphase generated to prevent electron transfer across the cathode–electrolyte interface. To understand interphase integrity over time, we interrogated Li|NMC811 cells after formation that had been further subjected to a charge current density of 1 mA cm⁻² and a high-power discharge current density of 6 mA cm⁻². After 50 cycles, we allowed the cells to rest for 24 h to investigate passivating character of interphase, i.e., in the absence of an applied potential (**Figure 2e**). We found that cells implementing LSCEs containing LiFSI alone or in combination with LiFSI or LiBF₄ showed rapid voltage drops during this period of observation. Cells implementing FC91, FD91, and FO91 showed steady cell voltage ~4.30 V vs. Li/Li⁺, while cells implementing FP91 and FT91 each experienced slow voltage fade. We repeated this sequence until the cells exhibited rapid voltage fade, or alternatively were invariant in their demonstrated stability. During these further investigations, LSCEs FC91 and FD91 emerged as superior, with less than 80 mV fade overall and less than 3.5 mV h⁻¹ fade rate.

In all cases other than FC91 and FD91, once a rapid voltage fade sets in, we observed a voltage fade to value that is less than the equilibrium voltage of a discharged Li|NMC811 cell (~3.2 V vs. Li/Li⁺). This indicates that NMC811 is undergoing further reduction—chemically, not electrochemically. There are two potential mechanisms explaining over-reduction of NMC811 in Li|NMC811 cells: a soft short, or an internal redox shuttle of electrons between anode and cathode. We ruled out soft-shorting since none of the cells experienced infinite-charging during the experiments. Instead, we found that cathodes were consistently recharged to their expected capacities and voltages in advance of the voltage fade during the rest period. This reversibility pointed to an internal shuttle as the origin of the behavior. The identification of an internal redox shuttle in electric aircraft-inspired Li|NMC811 cells featuring single-

anion and some mixed-anion LSCEs, but not others (i.e., FC91 and FD91), is intriguing for its apparent correlation to the stability and passivating character of the cathode–electrolyte interphase (CEI) (**Figure 2a–d**). For example, if the internal redox shuttle is mediated by metals in the electrolyte generated from NMC811, then the CEI plays a larger role than expected in preventing NMC corrosion. Furthermore, the passivating character of the anode SEI is called into question when a redox shuttle is observed in those select cases.

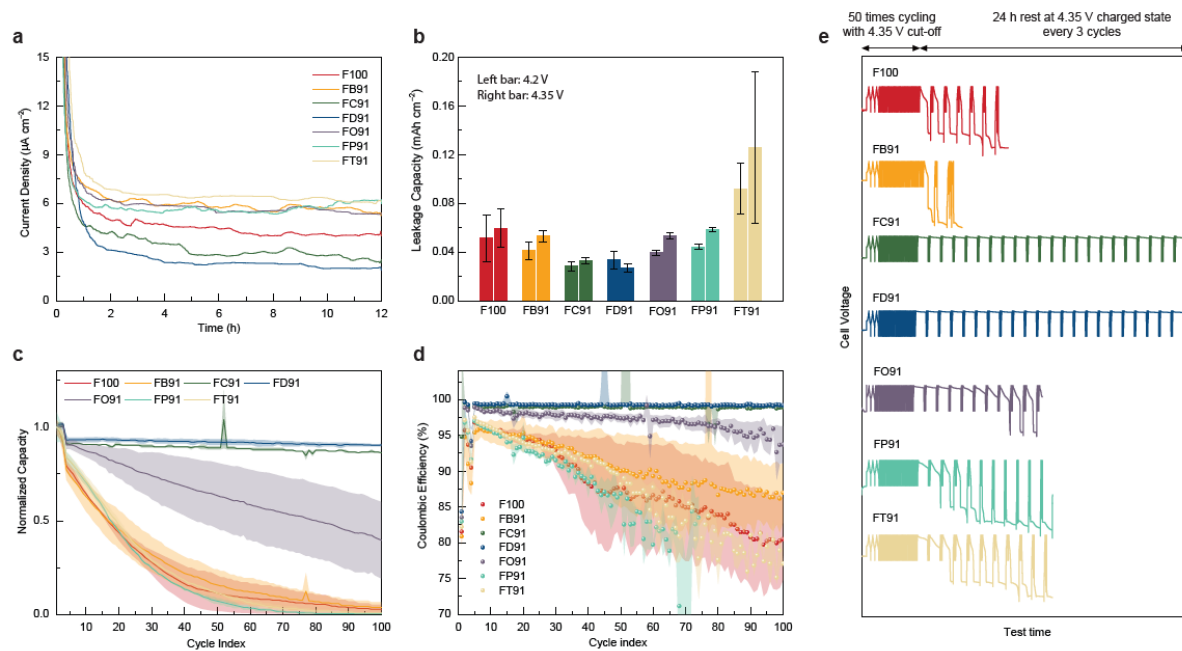


Figure 2. Single- and Mixed-Anion LSCE compatibility with NMC811 at high voltage. **a**, Leakage current density measured at the cell voltage of 4.35 V using Li|NMC811 full cells with LSCEs. **b**, Leakage capacity from leakage current accumulated over 10 h at a cell voltage of either 4.2 V or 4.35 V. **c**, Capacity retention of NMC811|NMC811 symmetric cells cycled with LSCEs. **d**, CE evolution during galvanostatic cycling of NMC811|NMC811 cells. **e**, Cell voltage profiles of Li|NMC811 cells during self-discharge experiments. Data are presented as the mean and standard deviation of three independent trials.

Lithium metal anode lifetime with mixed-anion LSCEs

We next set out to understand the chemistry of the anode SEI as well as the action of single- and mixed-anion LSCEs on Li plating and stripping in the absence of the NMC811 cathode. This is often done by reporting the Coulombic efficiency (*CE*), however, *CE* is not an intrinsic characteristic of an electrolyte, but rather extrinsic to the cell and its cycling protocol. To align with similar measurements in the field, we preconditioned the Cu electrode in a Li|Cu cell prior to depositing a Li reserve (4 mAh cm^{-2}), from which we reversibly stripped and re-plated 1 mAh cm^{-2} for 10 cycles at prescribed current densities (0.5 mA cm^{-2} and 0.5 mA cm^{-2} , respectively); we then stripped the remaining Li, evidenced by a voltage spike, concluding the experiment (**Figure 3a**). By comparing the capacity of Li plated in the initial reserve to what was stripped at the end of this sequence, we quantified *CE* for all LSCEs as well as a dilute electrolyte (1.0 M LiFSI in DME) to serve as a control. With the exception of FB91, all LSCEs showed higher *CE* (99.23–99.94%) than the dilute electrolyte (98.97%). These values are competitive with *CE* reported elsewhere by this method.²⁹

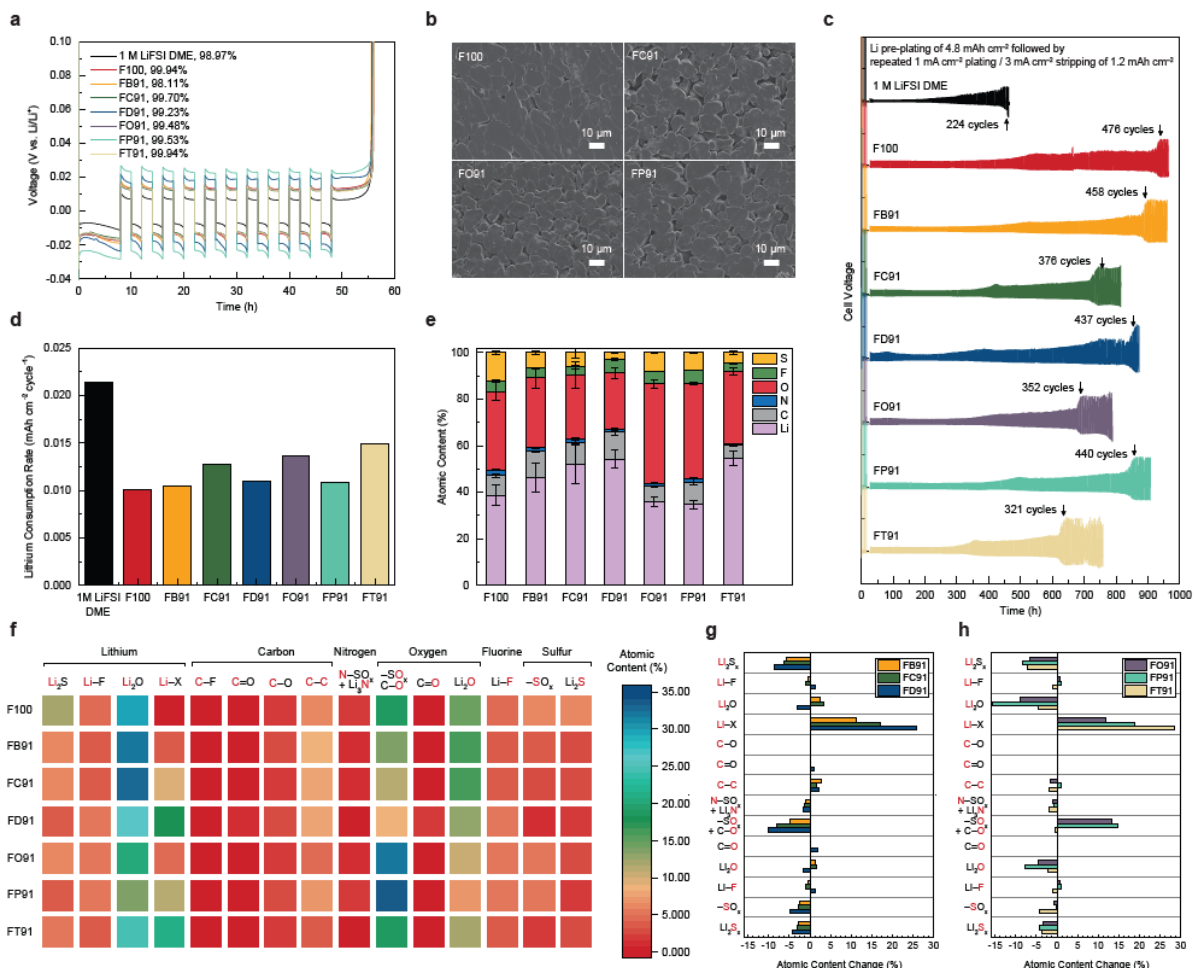


Figure 3. Single- and Mixed-Anion LSCE compatibility with Li metal. **a**, *CE* measurements in Li|Cu cells. **b**, SEM images of Li surface after 10 times of repeated Li plating and stripping with LSCEs with the current density of 0.5 mA cm^{-2} and the areal capacity of 1.0 mAh cm^{-2} . **c**, Cell voltage profile of Li|Cu cells with LSCEs during LCR test. **d**, Calculated LCR from (c) **e**, Atomic content in Li metal surface cycled under the same condition as (b) collected from XPS survey scan. **f**, Atomic percent for Li-, C-, N-, O-, F-, and S-containing components in the SEI obtained after XPS deconvolution. **g**, Up-regulated and down-regulated SEI components derived from FB91, FC91, and FD91 relative to the wild type, F100. **h**, Upregulated and downregulated SEI components derived from FO91, FP91, and FT91 relative to the wild type, F100.

We next imaged the Li surface after 10 cycles of plating and stripping (**Figure 3b** and **Supplementary Figure 5**) and found that the morphology Li was largely planar for LSCEs F100, FB91, and FT91, whereas features on a length scale of 10s of μm were evident for LSCEs FC91, FD91, FO91, and FP91. Across the lifetime of the cell, as the Li anode undergoes changes in morphology, the extent and rate of surface reactions, which scale with surface area, can be affected. To understand how single-anion and mixed-anion LSCEs dictate the time-averaged Li consumption rate (*LCR*) over the entire anode lifetime, we assembled Li|Cu cells and preconditioned the Cu electrodes, thereafter depositing 4.8 mAh cm^{-2} of Li. We then stripped from the reserve 1.2 mAh cm^{-2} at a current density of 6 mA cm^{-2} to simulate high-power discharge in cells for electric aircraft. We replated at 1 mA cm^{-2} and continued with this sequence until we observed a voltage spike, indicating the Li reserve was consumed (**Figure 3c**). From these data, we calculated *LCR* (**Figure 3d**). Relative to the dilute electrolyte, where anode lifetime was short (<450 h) and *LCR* high ($21 \mu\text{Ah cm}^{-2} \text{ cycle}^{-1}$), LSCEs demonstrated longer lifetime (650–925 h) and lower *LCRs* ($10\text{--}15 \mu\text{Ah cm}^{-2} \text{ cycle}^{-1}$).

We next turned to omics to develop an understanding for how changes in electrolyte composition produce changes in interphase chemistry ultimately dictating *CE* and *LCR*. We characterized by X-ray photoelectron spectroscopy (XPS) the chemical diversity in SEIs derived from single- and mixed-anion

LSCEs. Through deconvolution of energy-resolved XPS data and apportionment to specific chemical motifs based on known standards, we gained a holistic perspective of the “interphase-ome” for each electrolyte. If we define F100 as the “wild type”, by reference to the language of biologists, we can normalize the data accordingly and assess the extent to which specific chemistries in the interphase are “upregulated”, “downregulated”, or remain unchanged. Differences in composition will reflect changes in anion and solvent activity at the electrode–electrolyte interface, where such divergences are dictated by speciation in the clustered electrolytes as well as the structure of the inner Helmholtz layer when a voltage is applied to the cell.³⁴

For FC91, FD91, and FT91, the atomic percent for Li was higher than that for F100 and that this increase in Li content was concomitant with a lower atomic percent for O (**Figure 3e**). We found notable changes in the chemistry of oxygenated species in the SEI. Two species—SO_x and Li₂O—dominate the O1s spectra. Relative to F100, LSCEs FB91, FC91, and FD91 showed lower SO_x content, by as much as 46%, with subtle variations in Li₂O; FO91 and FP91 showed higher SO_x content, by as much as 73%, along with considerable Li₂O depletion (**Supplementary Figure 6** and **Supplementary Table 1-2**). The carbon atomic percent varied between 5.6–11.3%; 56.3–78.6% of this was attributed to aliphatic carbon species, rather than fluorocarbons; this indicated that DME is the primary contributor to carbon-containing compounds in the SEI. Interestingly, the nitrogen and sulfur content in the SEI decreased from 14.58% to as little as 3.75% in mixed-anion LSCEs relative to F100, suggesting markedly lower FSI[−] activity at Li metal in mixed-anion LSCEs, or preferential reactivity of the second anion in SEI generation. The fluorine content varied between 3.4–5.7% in single anion and mixed-anion LSCEs and was almost entirely accounted for by LiF.

Li|NMC811 cell performance under high-power and high-voltage cycling

The picture coming into focus is that mixed-anion LSCEs containing LiFSI and either LiClO₄ or LiDFOB form ionically conductive yet electronically passivating interphases at NMC811 when charged to 4.35 V vs. Li/Li⁺. These interphases plug the leakage current tied to electrolyte decomposition and

internal redox shuttles. In addition, Li anodes are long-lasting when these LSCEs are in place, even under demanding high-power cycling protocols. To understand how these phenomena and behaviors might be exploited to advance Li|NMC811 cells for electric aircraft beyond the state of the art, we tested power capability of the cells (**Supplementary Figure 7**) on discharge ($1\text{--}9 \text{ mA cm}^{-2}$) with fixed charge current density of 1 mA cm^{-2} . Single- and mixed-anion LSCEs showed similar rate capability with only $\sim 15\%$ capacity decrease as the current density was increased from 1 mA cm^{-2} ($\sim 0.7 \text{ C}$) to 9 mA cm^{-2} ($\sim 6 \text{ C}$). Similar experiments with a dilute electrolyte (1.0 M LiFSI in DME) confirmed limited power capability: $\sim 65\%$ capacity decrease between discharge rates of 0.7C and 6C (**Supplementary Figure 7**).

In extended cycling experiments, we found the advantages afforded by FC91 and FD91 were sustainable in Li|NMC811 cells operating at high power (6 mA cm^{-2}) (**Figure 4a–f** and **Supplementary Figures 8 & 9**). Cells implementing FC91 retained $\sim 90\%$ capacity after 500 cycles ($CE_{\text{avg}} = 99.976\%$) when charging to 4.2 V and $\sim 60\%$ when charging to 4.35 V ($CE_{\text{avg}} = 99.889\%$). Similarly, cells implementing FD91 retained $\sim 70\%$ capacity after 500 cycles when charging to 4.2 V ($CE_{\text{avg}} = 99.915\%$) and $\sim 70\%$ when charging to 4.35 V ($CE_{\text{avg}} = 99.928\%$). These outcomes are in contrast to the performance of cells assembled with F100, particularly when charged to 4.35 V: whereas $\sim 70\%$ capacity was retained after 300 cycles when charging to 4.2 V ($CE_{\text{avg}} = 99.887\%$), only 50% of the capacity was retained after 300 cycles when charging to 4.35 V ($CE_{\text{avg}} = 99.789\%$). We also found that cells implementing FC91 retained $\sim 70\%$ capacity after 1000 cycles when the constant voltage step was removed from charging protocol (**Supplementary Figure 10**). We further noted that LiBF₄, LiOTf, LiPF₆, and LiTFSI were inferior additives in mixed-anion LSCEs, consistent with their inability to electronically passivate NMC811 (**Figure 2**). We discerned from the charge and discharge curves that those for FC91 and FD91 exhibited the slowest rise in area-specific resistance (*ASR*) (**Figure 4c,f**). In cells whose capacity faded, this behavior was preceded by large increases in *ASR*. For cells implementing FB91 and FO91, the rise in *ASR* even led to soft shorts, evidenced by infinite charging. Discharging the cells at lower current density did not significantly change this analysis (**Supplementary Figure 11**).

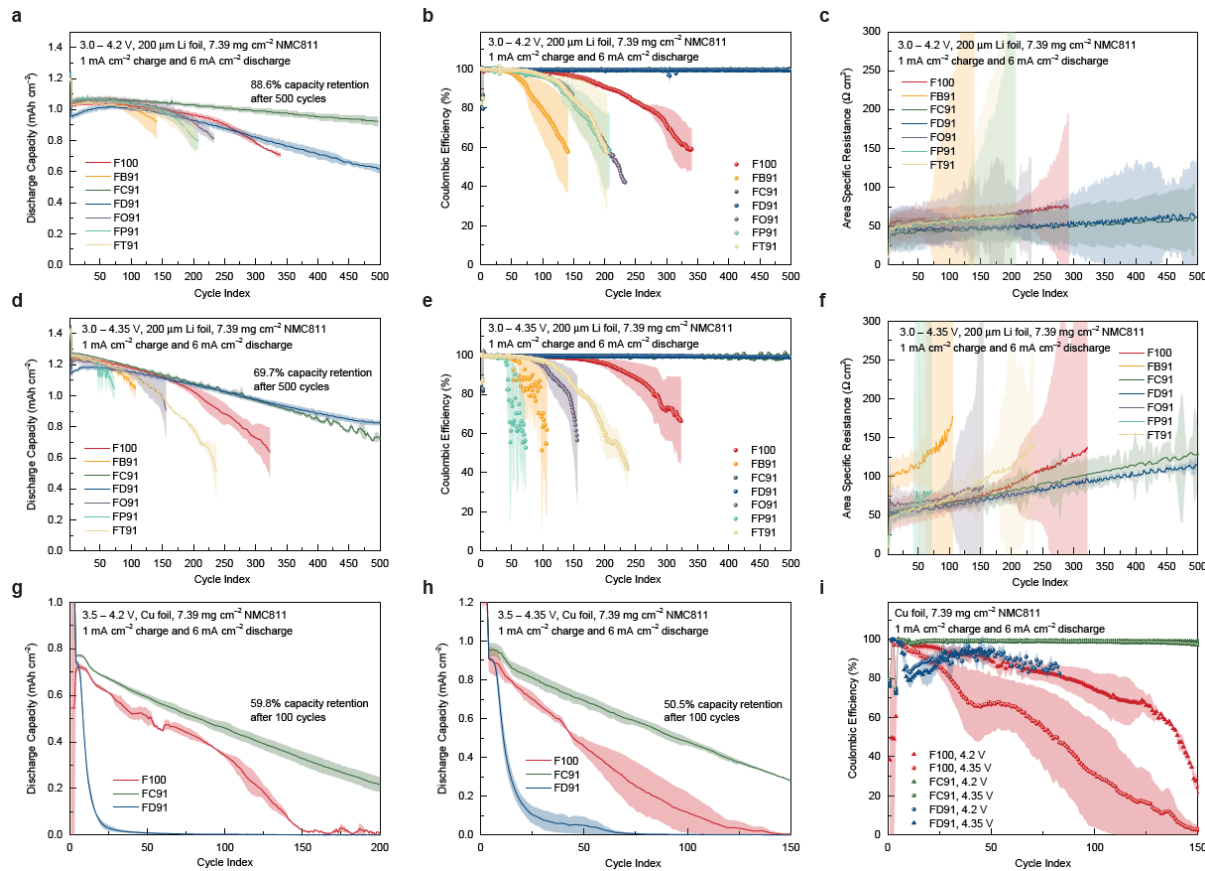


Figure 4. Full cell cycling performance with LSCEs. **a–c**, Capacity retention (**a**), *CE* (**b**), and *ASR* evolution (**c**) during the cycling of Li|NMC811 full cells with LSCEs under the charge cut-off voltage of 4.2 V and 1 mA cm⁻² charge current density and 6 mA cm⁻² discharge current density. **d–f**, Capacity retention (**d**), *CE* (**e**), and *ASR* evolution (**f**) during the cycling of Li|NMC811 full cells with LSCEs under the charge cut-off voltage of 4.35 V and 1 mA cm⁻² charge current density and 6 mA cm⁻² discharge current density. **g–i**, Capacity retention with the charge cut-off voltage of 4.2 V (**g**) and 4.35 V (**h**), and *CE* (**i**) during the cycling of Cu|NMC811 anodeless cells with F100, FC91, and FD91. Data are presented as the mean and standard deviation of three independent trials.

We compared the performance of Li|NMC811 cells featuring LSCEs FC91 and FD91 to those implementing standard-bearers, including fluoroether and fluorocarbonate LSCEs as well as various

dilute and concentrated dual-salt electrolytes (**Supplementary Table 3** and **Supplementary Figure 12**). Whereas mixed-anion LSCEs showed 70% capacity retention after 500 cycles of high power and high voltage cycling, the best of these reference electrolytes (RE1) showed capacity retention of 70% after only 330 cycles. Several reference electrolytes—including RE5, RE6, and RE7—even showed lower (14–21%) accessible capacities on discharge when compared to mixed-anion LSCEs.

Together, these data point to several conclusions. Impedance rise in conventional LSCEs implementing LiFSI alone as well as dilute and concentrated dual-salt electrolytes presents challenges long term for Li|NMC811 cells designed for electric aircraft, where high power on discharge and high voltage on charge are required. Specific mixed-anion LSCEs FC91 and FD91 provide advantages toward meeting those requirements, whereas others do not. In cases where LSCEs fail, this behavior is tied to insufficient stability and passivation of cathode and anode. In select instances, e.g., FB91, FO91 and FT91, infinite charge and slow self-discharge associated with the internal redox shuttle eventually takes hold, which are likely concomitant with the formation of soluble redox mediator (**Figure 3e**).

One explanation for this behavior is cathode degradation to soluble metal ions. Transition metal dissolution from NMC cathodes in Li-ion and lithium metal batteries cycled to high potential has been observed previously. Cathode impedance typically increases with the extent of dissolution. Furthermore, transition metal dissolution in turn leads to chemisorption of metal ions on the anode, where the metals undergo reduction. Once reduced, they trigger SEI and electrolyte decomposition, which further contributes to the overall impedance rise. Our results are consistent with these observations made with conventional electrolytes. Our data further suggest, however, that for some mixed-anion LSCEs, insufficient electronic passivation of anode and cathode permits an internal redox shuttle mediated by dissolved transition metals, which accelerates degradation of anode and cathode.

If anode–cathode crosstalk is mitigated and cycle-life extended in Li|NMC811 cells that use FC91 and FD91, then these advantages could be exploited in higher energy density cells with lower N/P ratio, where the Li inventory is in short supply. To test this, we assembled anodeless cells incorporating single- or mixed-anion LSCEs F100, FC91, or FD91 and cycled them with a charge current density of 1 mA

cm^{-2} and a discharge current density of 6 mA cm^{-2} ; in separate experiments, we implemented charge cut-off voltages of either 4.2 V or 4.35 V (**Figure 4g–i**). $\text{Cu}|\text{NMC811}$ cells incorporating FC91 showed the highest capacity retention, $\sim 60\%$ after 100 cycles with the 4.2 V cut-off ($CE_{\text{avg}} = 99.487\%$) and $\sim 51\%$ after 100 cycles with the 4.35 V cut-off ($CE_{\text{avg}} = 99.319\%$), while control cells incorporating F100 showed capacity retention of $\sim 48\%$ after 100 cycles with the 4.2 V cut-off ($CE_{\text{avg}} = 99.266\%$) and $\sim 13\%$ after 100 cycles with the 4.35 V cut-off ($CE_{\text{avg}} = 97.974\%$). From the charge and discharge profiles, none of the cells experienced infinite-charging. Interestingly, while $\text{Li}|\text{NMC811}$ cells incorporating FD91 showed outstanding performance, $\text{Cu}|\text{NMC811}$ cells incorporating FD91 exhibited faster capacity fade than both FC91 and F100. Thus, in $\text{Li}|\text{NMC811}$ cells, where the Li inventory is in excess, LiDFOB is adept in passivating cathode, preventing both continuous electrolyte degradation and transition metal dissolution, which in turn extends their cycle life. In $\text{Cu}|\text{NMC811}$ cells, however, where the failure mechanism is tied to anode reversibility, the Li inventory is mismanaged and irrevocably lost. This observation is surprising, considering the efficacy of LiDFOB alongside LiBF_4 in concentrated dual-salt carbonate electrolytes.³⁵ There is much to learn of the influence of ion-solvation environments governing reactivity in mixed-anion electrolytes, whether they are concentrated, super-concentrated, or locally super-concentrated. Nevertheless, we conclude from these experiments that mixed-anion LSCEs incorporating LiFSI and LiClO_4 provide an intriguing avenue for sustained electronic passivation of both anode and cathode in $\text{Li}|\text{NMC811}$ cells designed for high power and high energy density, regardless of the N/P ratio.

Origins of Anode–Cathode Crosstalk in $\text{Li}|\text{NMC811}$ Cells

To understand the origins of anode–cathode crosstalk and associated *ASR* increase, which portends cell failure, we disassembled $\text{Li}|\text{NMC811}$ cells driven on charge to a voltage cut-off of 4.35 V after cycle 250. For cells implementing single-anion F100, the Li anode extracted revealed extensive accumulation of a black-colored material (**Figure 5a** and **Supplementary Figures 13 & 14**), enriched with degradation products of FSI^- relative to what they would be in the absence of the influence of the

cathode (**Supplementary Figure 15**). This residue was also present on both sides of the separator. SEM/EDX analysis of this material, which does not form in Li|Li symmetric cells, evidenced transition metals, including nickel (**Supplementary Figure 16**). This observation is consistent with previous reports, in which transition metal dissolution from the cathode was concomitant with anode fouling, in the present case, from FSI^- redox. This residue was less pronounced in cells implementing FC91 and FD91 (**Figure 5a**). Interestingly, an Li|NMC811 cell rebuilt with the extracted F100 anode regained nearly all of its capacity, whereas a cell rebuilt with the extracted cathode continued to lose capacity (**Figure 5b**). This indicates that in Li|NMC811 cells, capacity loss and cell failure is dictated by cathode degradation, even though when transition metals appear in the SEI, build-up of residue on Li is also observed (**Supplementary Figures 13 & 14**). Similar experiments where retrieved cathodes were assembled into Cu|NMC811 cells confirmed that cathode degradation with F100 is permanent, progressive, and therefore deleterious to cell health, whereas cathodes cycled with FC91 and FD91 were stable and resilient (**Supplementary Figure 17**).

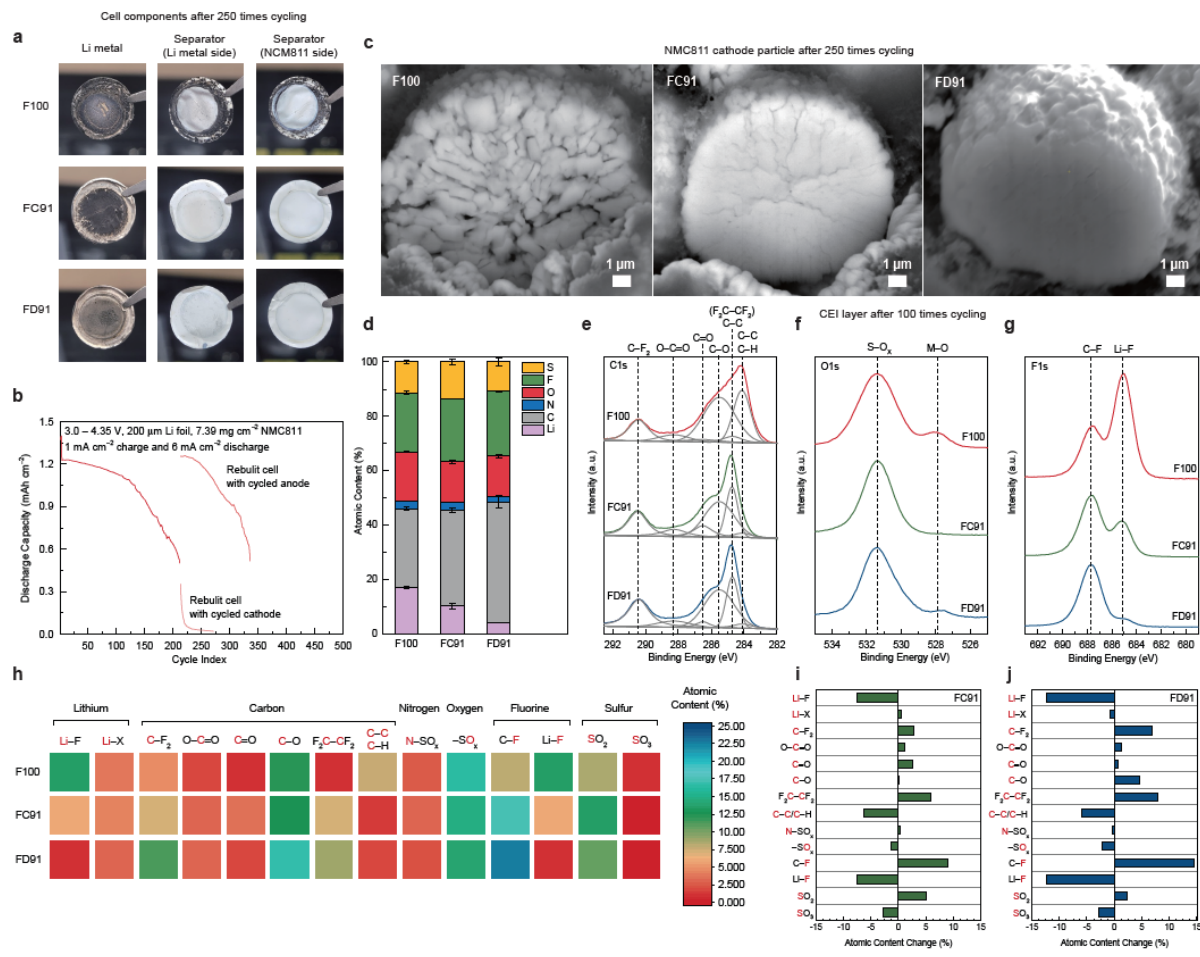


Figure 5. Degradation behavior of Li|NMC811 full cells during the cycling with LSCEs. **a**, Images of cell components from the disassemble Li|NMC811 full cells after cycling 250 times with F100, FC91, and FD91. **b**, Capacity retention of fresh Li|NMC811 full cells with F100, and rebuilt Li|NMC811 cells assembled with cycled anode/fresh cathode or fresh anode/cycled cathode using F100. **c**, FIB-SEM cross-sectional images of NMC811 secondary particles 250 times cycled in Li|NMC811 full cells with F100, FC91, and FD91. **d**, Atomic content ratio from XPS data collected from NMC811 cathode 100 times cycled with F100, FC91, and FD91. **e–g**, C1s (**e**), O1s (**f**), and F1s (**g**) XPS spectra collected from NMC811 cathode 100 times cycled with F100, FC91, and FD91. **h**, Atomic percent for Li-, C-, N-, O-, F-, and S-containing components in the CEI obtained after XPS deconvolution. **i**, Upregulated and downregulated CEI components derived from FC91 relative to the wild type, F100. **j**, Upregulated and downregulated CEI components derived from FD91 relative to the wild type, F100.

We imaged using FIB-SEM NMC811 cathodes in cross-section taken from Li|NMC811 cells at cycle 250 that used either F100, FC91, or FD91 as the LSCE (**Figure 5c**). For F100 cells, we observed extensive fracturing of the 10- μm secondary NMC particles into sub- μm primary particles. This explains capacity loss in those cells: fracturing over time initially causes *ASR* to rise in advance of electronic isolation and precipitous capacity loss. Cathode fracturing also explains our observations of high rates of self-discharge with F100, since fresh surface area is being exposed. When the electrolyte degrades during self-discharge, the build-up of material between primary particles likely produces tensile stress at the associated grain boundaries, initiating a crack that propagates along the grain boundary, which in turn leads to fracture and electronic isolation. In sharp contrast, NMC811 particles cycled with FD91 do not show signs of fracturing, e.g., by reference to pristine NMC811 (**Supplementary Figure 18**) and NMC particles cycled with FC91. This explains why *ASR* rise is slow and capacity retention high in Li|NMC811 cells cycled to high voltage and delivering high power on discharge with FC91 and FD91.

To understand the origins of electronic passivation in CEIs derived from FC91 and FD91 relative to the F100 wild type, we turned again to interphase-omics. We characterized CEIs derived from F100, FC91, and FD91 by XPS using cathodes extracted from Li|NMC811 cells after cycle 100 (**Figure 5d-i**, **Supplementary Figure 19** and **Supplementary Table 4-5**). Relative to F100, CEIs derived from FC91 and FD91 were expectedly enriched with organics (e.g., C–H/C–C, C–F, and C–O) by up to ~50% and depleted in inorganics (e.g., LiF, Li₂O, and to a lesser extent LiSO_x) by up to ~75%. While the range of atomic F content is narrow for all LSCEs (23–26%), exclusive to mixed-anion LSCEs, we see dramatic shifts from LiF to C–F bonding in the CEIs: for example, from ~64% LiF in F100 to less than 5% in FD91. We found that these increases in C–F content were concomitant with increases in CF₂–CF₂ (from 1.3% in F100 to 9.7% in FD91) and C–O (from 13% in F100 to 18% in FD91) in the C1s and O1s spectra, but decreases in aliphatic C–H and C–C bonding (from 8.2% in F100 to 1.8% in FD91). Because these bonds are exclusive to DME and TTE, our observations indicate that the activity of DME

is lower at the cathode while that for TTE is higher in mixed-anion LSCEs containing LiFSI and either LiClO₄ or LiDFOB relative to the activities observed when using a single-anion LSCE. Furthermore, we observe that integration of CEI components derived from enhanced TTE decomposition relative to DME in mixed-anion LSCEs protects against cathode corrosion, which in turn delays the onset of fracturing indefinitely. To contextualize the advance, it was known for LSCEs featuring LiFSI, DME, and TTE that TTE decomposition at NMC811 creates a CEI that prevents over-oxidation of DME. However, in offering mixed-anion LSCEs to more broadly tailor DME and TTE activity at the cathode, we provide new routes for CEI engineering for stabilizing the cathodes against degradation at high voltage in anodeless and Li metal cells, including those designed for electric aircraft.

Conclusion

Cathode degradation, fracturing, and electronic isolation have long been a problem for Li-ion, lithium metal, and anodeless cells featuring polycrystalline NMC active materials. Coating the surfaces of NMC particles *ex-situ* (i.e., in advance of cathode fabrication) has not yet provided lasting protection against degradation. This has led the field to consider NMC defect engineering and doping with metals, whose purported benefits are difficult to realize when charging to high voltage. Our observations that mixed-anion LSCEs address NMC degradation by *in-situ* formation of a stabilizing fluoroether-rich interphase is intriguing and likely more general and straightforward to execute at scale. Furthermore, we gain fundamental insights into the origins of CEI stability by introducing omics into the discovery and development phase of advanced electrolytes. Specifically, we find that LiClO₄ and LiDFOB reduce the activity of DME at the cathode during CEI generation, such that it becomes enriched with organics arising from enhanced TTE decomposition. The benefits of mixed-anion LSCEs are noted in both lithium metal and anodeless cells operating at high voltage and high power, pointing to their use in electric aircraft. Because chemical space is vast, we anticipate that future iterations of the mixed-anion LSCE platform will provide an opportunity to tailor electrolytes for different battery chemistries, while also considering their anticipated missions. Electrolyte design and discovery will in the future be aided

by autonomous workflows encompassing robotics, machine learning and AI. Integrating advanced characterization and omics into these workflows serves to build a robust knowledge base of electrolyte reactivity in electrochemical systems, where complexity is embraced and exploited, accelerating technology development to meet the urgent demands for deep decarbonization through electrification.

Methods

Materials. LiFSI (Gotion), LiBF₄ (Sigma-Aldrich), LiClO₄ (Sigma-Aldrich), LiDFOB (Sigma Aldrich), LiOTf (Sigma-Aldrich), LiPF₆ (Strem Chemicals), LiTFSI (Gotion) were dried at 60 °C under vacuum for at least 12 h. DME (Gotion), TTE (SynQuest), dimethyl carbonate (Sigma-Aldrich), diethyl carbonate (Sigma-Aldrich), *bis*(2,2,2-trifluoroethyl)ether (Sigma-Aldrich), *tris*(2,2,2-trifluoroethyl)orthoformate (Synquest), fluoroethylene carbonate (Sigma-Aldrich) were degassed with Ar and dried over activated 4-Å molecular sieves. A standard battery electrolyte comprising 1.0 M LiPF₆ in EC/DMC (1:1 by weight) was purchased from Sigma-Aldrich and used as received. Electrolytes were prepared in an Ar-filled glove box (H₂O < 0.5 ppm, O₂ < 0.5 ppm) by dissolving the lithium salt(s) into the coordinating solvent(s); for LSCEs, these solutions were combined with fluorinated diluents in the prescribed quantities. NMC811 electrodes (7.39 mg cm⁻²) were supplied by the CAMP facility at Argonne National Laboratory. PE separators were sourced from Wscope. Li metal foil (200 µm) was sourced from Honjo. CR2032 coin cell components, including Al-coated bottom cases, were sourced from Hohsen.

Characterization. Electrolyte conductivity was measured at 22.7–23.2 °C using a Mettler Toledo Seven2Go conductivity meter. Raman spectra were collected using a Shimadzu Labram 2000 equipped with a 532-nm laser. XPS spectra were collected using a Thermo-Fisher K-Alpha Plus; samples were transferred from Ar-filled glove box to XPS using air-free vacuum transfer module. Peak deconvolution of XPS spectra was conducted by XPSPEAK41. SEM of Li anodes were conducted using Zeiss Gemini Supra 55 VP-SEM. SEM/EDX analysis of Li anode surface was conducted using EDAX Octane Super detector, installed to Helios G4 UX Dual Beam FIB–SEM (FEI/Thermo Fisher). To prevent the contamination on Li metal anode surface during the sample transfer for the SEM/EDX analysis, an air-

tight sample transfer module (Kammrath and Weiss Technologies) was used. Microstructure changes in NMC811 were observed in SEM from images obtained after cross-sectioning the particles using a Scios Dual Beam FIB–SEM (FEI/Thermo Fisher). Specifically, the cathode particles were cross-sectioned utilizing the Ga^+ ion beam. The particles were milled with a beam current of 0.9–6.5 nA and then polished with a beam current of 93 pA to 0.46 nA.

Electrochemistry.

Instrumentation, Electrolyte preparation and electrochemical cells were assembled in an Ar-filled glove box ($\text{H}_2\text{O} < 0.5 \text{ ppm}$, $\text{O}_2 < 0.5 \text{ ppm}$). LSV experiments were conducted using a Biologics VMP3. Potentiostatic and galvanostatic cycling experiments were conducted using an Arbin LBT20084 potentiostat. All experiments were conducted in a temperature-controlled oven (25 °C).

Cell assembly, Li|Al CR2032 coin cells were assembled using Al foils (19-mm diameter), PE separators (16-mm diameter), and Li foils (12-mm diameter). Li|NMC811 CR2032 coin cells were assembled with Li foils (14-mm diameter), PE separators (16-mm diameter), and NMC811 cathodes (12-mm diameter). In advance of assembling NMC811|NMC811 CR2032 coin cells, one of the NMC811 electrodes was first charged in an Li|NMC811 cell using a CCCV protocol with the constant current of 0.3 mA cm⁻² to 4.35 V followed by CV step with the cut-off current density of 0.03 mA cm⁻² and a time cut-off of 1 h. Charged NMC811 cathodes from those cells were retrieved and re-assembled with pristine NMC811 electrodes (12-mm diameter) and PE separators (16-mm diameter). Li|Cu CR2032 coin cells were assembled using Cu foils (19-mm diameter), PE separators (16-mm diameter), and Li foils (12-mm diameter). Cu|NMC811 CR2032 coin cells were assembled in a similar manner, replacing Li foils with Cu foils (19-mm diameter). For all cells, 30 µL of electrolyte was used.

Linear sweep voltammetry test, LSV was carried out in Li|Al CR2032 coin cells across a voltage range of 2.0 V to 6.0 V at a rate of 1 mV s⁻¹.

Leakage current tests, Leakage current experiments were conducted in Li|NMC811 CR2032 coin cells

equilibrated for at least 12 h to distribute the electrolyte. Cells were initially charged to 4.2 V at 0.1 mA cm⁻², after which the current over time was observed for 12 h while being driven at that voltage. Cells were then charged to 4.35 V at 0.1 mA cm⁻², after which the current over time was observed for an additional 12 h while being driven at that voltage.

NMC symmetric cell tests, NMC811|NMC811 CR2032 coin cells were cycled using a CCCV protocol between 1.2 V and -1.2 V. Formation was carried out over three cycles using a CCCV protocol at a constant current density of 0.3 mA cm⁻² as well as a current density cut-off of 0.03 mA cm⁻² and time cut-off of 1 h during the CV step. After formation, cells were cycled using a CCCV protocol at a constant current density of 1 mA cm⁻² as well as a current density cut-off of 0.1 mA cm⁻² and time cut-off of 1 h during the CV step.

Self-discharge tests, Formation was carried out over three cycles on Li|NMC811 CR2032 coin cells using the same CCCV protocol used for the galvanostatic cycling tests, using 4.35 V as the upper cutoff voltage and 3.0 V as the lower cutoff voltage. After formation, cells were cycled at the higher current densities, also as described. Cells were monitored in their charged state for 24 h every three cycles.

Coulombic efficiency tests, Preconditioning Li|Cu CR2032 coin cells was carried out by plating 4.0 mAh cm⁻² of Li onto the Cu foils at a current density of 0.5 mA cm⁻² and then stripping it at a current density of 0.5 mA cm⁻² until a voltage cutoff of 1.0 V. A reservoir comprising 4.0 mAh cm⁻² of Li was then plated onto the Cu foils at a current density of 0.5 mA cm⁻², after which 1.0 mAh cm⁻² was reversibly stripped and plated at a current density of 0.5 mA cm⁻² for 10 cycles. The remaining Li on Cu was then stripped at a current density of 0.5 mA cm⁻² until a voltage cutoff of 1.0 V.

Li consumption rate test, Preconditioning Li|Cu CR2032 coin cells was carried out by plating 1.2 mAh cm⁻² of Li onto the Cu foils at a current density of 0.5 mA cm⁻² and then stripping it at a current density of 0.5 mA cm⁻² until a voltage cutoff of 1.0 V. A reservoir comprising of 4.8 mAh cm⁻² (Q_T) of Li then was plated onto the Cu foils at a current density of 0.5 mA cm⁻², after which 1.2 mAh cm⁻² (Q_C) was reversibly stripped (3.0 mA cm⁻²) and plated (1.0 mA cm⁻²) for n cycles until a voltage cutoff of 0.5 V. Li consumption rates (LCR) were calculated according to the equation below.

$$LCR = \frac{Q_T - Q_C}{n} \quad (\text{Eq. 1})$$

Rate capability tests, Formation was carried out over six cycles on Li|NMC811 and Cu|NMC811 CR2032 coin cells using a CCCV protocol. During charge, a current density of 0.3 mA cm^{-2} was used along with a 4.2 V cutoff; this was followed by a CV step with current density cut-off of 0.03 mA cm^{-2} and time cut-off of 1 h. During discharge, a current density of 0.3 mA cm^{-2} was used along with a 3.0 V cutoff. After formation, cells were cycled using a similar CCCV protocol, changing the charge current density to 1 mA cm^{-2} , the current density cut-off during the CV step to 0.1 mA cm^{-2} , and the discharge current density to 1 mA cm^{-2} , 3 mA cm^{-2} , 6 mA cm^{-2} , 9 mA cm^{-2} , and 1 mA cm^{-2} in sequences of 3 cycles at each prescribed discharge current density.

Galvanostatic cycling tests, Formation was carried out over three cycles for Li|NMC811 and Cu|NMC811 CR2032 coin cells using a CCCV protocol. During charge, a current density of 0.3 mA cm^{-2} was used along with either a 4.2 V or 4.35 V cutoff; this was followed by a CV step with current density cut-off of 0.03 mA cm^{-2} and time cut-off of 1 h. During discharge, a current density of 0.3 mA cm^{-2} was used along with either a 3.0 V or 3.5 V cutoff. After formation, cells were cycled using a similar CCCV protocol, changing the charge current density to 1 mA cm^{-2} , the current density cut-off during the CV step to 0.1 mA cm^{-2} , and the discharge current density to 6 mA cm^{-2} .

Atomic content calculation from XPS spectrum

The intensity of photoelectrons from XPS spectra is given by:

$$I_a = N_a \sigma_a \lambda_a K$$

where I_i is intensity of photoelectron from element a , N_a is the atomic concentration of element a , σ_a is Scofield's relative sensitivity factor of element a , λ_a is inelastic mean free path of a photoelectron from element a , and K is a constant for all other equipment- and measurement-related factors assumed to be constant during experiment.

Therefore, the atomic content of element a from multi-component materials containing element

a, b, c, \dots can be calculated as follows:

$$\frac{N_a}{N_a + N_b + N_c + \dots} = \frac{\frac{I_a}{\sigma_a \lambda_a}}{\frac{I_a}{\sigma_a \lambda_a} + \frac{I_b}{\sigma_b \lambda_b} + \frac{I_c}{\sigma_c \lambda_c} + \dots}$$

Scofield's relative sensitivity factor, σ and inelastic mean free path, λ used for each element are as follows; $\sigma_{Li\ 1s} = 0.0568$, $\sigma_{C\ 1s} = 1.0$, $\sigma_{N\ 1s} = 1.8$, $\sigma_{O\ 1s} = 2.93$, $\sigma_{F\ 1s} = 4.43$, $\sigma_{S\ 2p(\frac{1}{2})} = 0.567$, $\sigma_{S\ 2p(\frac{3}{2})} = 1.11$, $\lambda_{Li\ 1s} = 45.8$, $\lambda_{C\ 1s} = 33.0$, $\lambda_{N\ 1s} = 29.2$, $\lambda_{O\ 1s} = 6.7$, $\lambda_{F\ 1s} = 23.0$, and $\lambda_{S\ 2p} = 29.9$.

Area-Specific Resistance Calculations

The area specific resistance (ASR) was calculated each cycle using the following relation:

$$ASR = \left(\frac{\left(\frac{E_{charge}}{Q_{charge}} - \frac{E_{discharge}}{Q_{discharge}} \right) \times A}{I_{charge} + I_{discharge}} \right)$$

where E_{charge} is the charge energy, $E_{discharge}$ is the discharge energy, Q_{charge} is the charge capacity, $Q_{discharge}$ is the discharge capacity, A is the cathode surface area, I_{charge} is the charge current, and $I_{discharge}$ is the discharge current.

The standard error for ASR was derived using error propagation rules.

$$\sigma_{ASR} = (Q_{charge}^4 Q_{discharge}^2 A^2 \sigma_{E_{discharge}}^2 (I_{charge} + I_{discharge}))^2 +$$

$$(Q_{charge}^4 A^2 E_{discharge}^2 \sigma_{Q_{discharge}}^2 (I_{charge} + I_{discharge}))^2 +$$

$$(Q_{discharge}^4 Q_{charge}^2 A^2 \sigma_{E_{charge}}^2 (I_{charge} + I_{discharge}))^2 +$$

$$(Q_{charge}^2 Q_{discharge}^2 A^2 (\sigma_{I_{charge}}^2 + \sigma_{I_{discharge}}^2) (Q_{charge} E_{discharge} - Q_{discharge} E_{charge}))^2 +$$

$$Q_{\text{charge}}^2 Q_{\text{discharge}}^2 \sigma_A^2 (I_{\text{charge}} + I_{\text{discharge}})^2 (Q_{\text{charge}} E_{\text{discharge}} - Q_{\text{discharge}} E_{\text{charge}})^2 + \\ Q_{\text{discharge}}^4 A^2 E_{\text{charge}}^2 \sigma_Q^2 (I_{\text{charge}} + I_{\text{discharge}})^2 \div \\ (Q_{\text{charge}}^4 Q_{\text{discharge}}^4 (I_{\text{charge}} + I_{\text{discharge}})^4)$$

Where $\sigma_{E_{\text{charge}}}$ is the standard deviation of charge energy, $\sigma_{E_{\text{discharge}}}$ is the standard deviation of discharge energy, σ_Q_{charge} is the standard deviation of charge capacity, $\sigma_Q_{\text{discharge}}$ is the standard deviation of discharge capacity, σ_A is the standard deviation of cathode area, σ_Q_{charge} is the standard deviation of charge current, and $\sigma_Q_{\text{discharge}}$ is the standard deviation of discharge current. The values for σ_A , $\sigma_Q_{\text{discharge}}$, and σ_Q_{charge} were assumed to be zero.

References

1. Viswanathan, V. *et al.* The challenges and opportunities of battery-powered flight. *Nature* **601**, 519–525 (2022).
2. Sripad, S. & Viswanathan, V. The promise of energy-efficient battery-powered urban aircraft. *Proc. Natl. Acad. Sci.* **118**, e2111164118 (2021).
3. Schäfer, A. W. *et al.* Technological, economic and environmental prospects of all-electric aircraft. *Nat. Energy* **4**, 160–166 (2019).
4. Xue, W. *et al.* Ultra-high-voltage Ni-rich layered cathodes in practical Li metal batteries enabled by a sulfonamide-based electrolyte. *Nat. Energy* **6**, 495–505 (2021).
5. Xu, R., Sun, H., de Vasconcelos, L. S. & Zhao, K. Mechanical and structural degradation of $\text{LiNi}_x\text{Mn}_y\text{Co}_z\text{O}_2$ cathode in Li-ion batteries: an experimental study. *J. Electrochem. Soc.* **164**, A3333 (2017).
6. Niu, C. *et al.* Balancing interfacial reactions to achieve long cycle life in high-energy lithium metal batteries. *Nat. Energy* **6**, 723–732 (2021).
7. Karczewski, K. J. & Snyder, M. P. Integrative omics for health and disease. *Nat. Rev. Genet.* **19**, 299–310 (2018).
8. Gehlenborg, N. *et al.* Visualization of omics data for systems biology. *Nat. Methods* **7**, S56–

S68 (2010).

9. Axsen, J., Plötz, P. & Wolinetz, M. Crafting strong, integrated policy mixes for deep CO₂ mitigation in road transport. *Nat. Clim. Change* **10**, 809–818 (2020).
10. Bouckaert, S. *et al.* Net Zero by 2050: A roadmap for the global energy sector. (2021).
11. Jiao, S. *et al.* Stable cycling of high-voltage lithium metal batteries in ether electrolytes. *Nat. Energy* **3**, 739–746 (2018).
12. Ren, X. *et al.* Enabling high-voltage lithium-metal batteries under practical conditions. *Joule* **3**, 1662–1676 (2019).
13. Cao, X. *et al.* Monolithic solid-electrolyte interphases formed in fluorinated orthoformate-based electrolytes minimize Li depletion and pulverization. *Nat. Energy* **4**, 796–805 (2019).
14. Chen, S. *et al.* High-voltage lithium-metal batteries enabled by localized high-concentration electrolytes. *Adv. Mater.* **30**, 1706102 (2018).
15. Yu, Z. *et al.* Rational solvent molecule tuning for high-performance lithium metal battery electrolytes. *Nat. Energy* **7**, 94–106 (2022).
16. Yu, Z. *et al.* Molecular design for electrolyte solvents enabling energy-dense and long-cycling lithium metal batteries. *Nat. Energy* **5**, 526–533 (2020).
17. Zhao, Y. *et al.* Fluorinated ether electrolyte with controlled solvation structure for high voltage lithium metal batteries. *Nat. Commun.* **13**, 2575 (2022).
18. Zhang, H. *et al.* Electrolyte additives for lithium metal anodes and rechargeable lithium metal batteries: progress and perspectives. *Angew. Chem., Int. Ed.* **57**, 15002–15027 (2018).
19. Tan, S. *et al.* Additive engineering for robust interphases to stabilize high-Ni layered structures at ultra-high voltage of 4.8 V. *Nat. Energy* **7**, 484–494 (2022).
20. Li, L. *et al.* Highly fluorinated Al-centered lithium salt boosting the interfacial compatibility of Li-metal batteries. *ACS Energy Lett.* **7**, 591–598 (2022).
21. Zhu, C. *et al.* Anion-diluent pairing for stable high-energy Li metal batteries. *ACS Energy Lett.* **7**, 1338–1347 (2022).
22. Chen, Y. *et al.* Steric effect tuned ion solvation enabling stable cycling of high-voltage lithium metal battery. *J. Am. Chem. Soc.* **143**, 18703–18713 (2021).
23. Wang, H. *et al.* Dual-solvent Li-ion solvation enables high-performance Li-metal batteries. *Adv.*

Mater. **33**, 2008619 (2021).

24. Amanchukwu, C. V. *et al.* A new class of ionically conducting fluorinated ether electrolytes with high electrochemical stability. *J. Am. Chem. Soc.* **142**, 7393–7403 (2020).
25. Xue, W. *et al.* FSI-inspired solvent and “full fluorosulfonyl” electrolyte for 4 V class lithium-metal batteries. *Energy Environ. Sci.* **13**, 212–220 (2020).
26. Dave, A. *et al.* Autonomous discovery of battery electrolytes with robotic experimentation and machine learning. *Cell Rep. Phys. Sci.* **1**, 100264 (2020).
27. Matsuda, S., Lambard, G. & Sodeyama, K. Data-driven automated robotic experiments accelerate discovery of multi-component electrolyte for rechargeable Li–O₂ batteries. *Cell Rep. Phys. Sci.* **3**, 100832 (2022).
28. Dave, A. *et al.* Autonomous optimization of nonaqueous battery electrolytes via robotic experimentation and machine learning. *arXiv preprint arXiv:14786* (2021).
29. Hobold, G. M. *et al.* Moving beyond 99.9% Coulombic efficiency for lithium anodes in liquid electrolytes. *Nat. Energy* **6**, 951–960 (2021).
30. Cao, X., Jia, H., Xu, W. & Zhang, J.-G. Localized high-concentration electrolytes for lithium batteries. *J. Electrochem. Soc.* **168**, 010522 (2021).
31. Lin, S., Hua, H., Lai, P. & Zhao, J. A multifunctional dual-salt localized high-concentration electrolyte for fast dynamic high-voltage lithium battery in wide temperature range. *Adv. Energy Mater.* **11**, 2101775 (2021).
32. Qian, J. *et al.* High rate and stable cycling of lithium metal anode. *Nat. Commun.* **6**, 6362 (2015).
33. Holoubek, J. *et al.* Tailoring electrolyte solvation for Li metal batteries cycled at ultra-low temperature. *Nat. Energy* **6**, 303–313 (2021).
34. Yan, C. *et al.* Regulating the inner Helmholtz plane for stable solid electrolyte interphase on lithium metal anodes. *J. Am. Chem. Soc.* **141**, 9422–9429 (2019).
35. Weber, R. *et al.* Long cycle life and dendrite-free lithium morphology in anode-free lithium pouch cells enabled by a dual-salt liquid electrolyte. *Nat. Energy* **4**, 683–689 (2019).

Acknowledgements

The information, data, or work presented herein was funded in part by the Advanced Research Projects Agency-Energy (ARPA-E), U.S. Department of Energy, under Award Number DE-AR0001450. The

views and opinions of authors expressed herein do not necessarily state or reflect those of the United States Government or any agency thereof. Work at the Molecular Foundry—including electron microscopy and X-ray spectroscopy—was supported by the Office of Science, Office of Basic Energy Sciences, of the U.S. Department of Energy under Contract No. DE-AC02-05CH11231. Cathodes were produced by B. Polzin, S. Trask, and A. Jansen at the US DOE CAMP (Cell Analysis, Modeling and Prototyping) Facility, Argonne National Laboratory. The CAMP Facility is fully supported by the DOE Vehicle Technologies Office. Dr. Jiwoong Bae is thanked for helpful discussions.

Author contributions

Y.K., M.A.B., and B.A.H. designed and B.A.H. directed the studies. Y.K. conducted the electrochemical studies. M.A.B. performed SEM of Li metal anodes and developed electroanalytical methods for tracking cell impedance. X.P. and T.O. obtained cross-sectional SEM images of cycled NMC cathodes under the supervision of M.C.S.. Y.-W.B. conducted SEM-EDX analysis on cycled Li metal anode under the supervision of H.K.. L.M.K. collected the XPS spectra. Y.K. and B.A.H. developed the interphase-omics approach. Y.K. and B.A.H. wrote first draft of the manuscript and all authors contributed to the final draft.

Competing interests

The authors declare the following competing interests: Y.K., M.A.B., and B.A.H. are co-inventors on US provisional patent application 63/184,759 submitted by Lawrence Berkeley National Laboratory that covers materials, components, and designs for high power batteries for electric vehicles and aircraft. B.A.H. has a financial interest in Sepion Technologies and Cyklos Materials.

Supplementary Tables

Supplementary Table 1. Raw data based on XPS survey scan collected from SEI on Li metal cycled in Li|Li symmetric cells

Integrated peak intensity from XPS survey scan							
Electrolyte	Li 1s	C 1s	N 1s	O 1s	F 1s	S 2p (1/2)	S 2p (3/2)
F100-1	119454.79	345670.8	191910.2	3951863	662392.6	144960.447	289920.893
F100-2	147495.15	394682.7	156117.4	3071279	558553.6	124592.483	249184.967
FB91-1	152055.77	554785.9	116748.4	3929442	665635.4	89352.2067	178704.413
FB91-2	127036.37	341746.5	57470.71	1861686	345913.5	47568.81	95137.62
FC91-1	144629.3	376827.1	114558.3	3311274	559663.2	91116.4067	182232.813
FC91-2	124289.43	278331.4	37912.84	1360608	206001.7	24907.4267	49814.8533
FD91-1	138352.4	465254.7	32789.31	2203463	691681.6	22636.0667	45272.1333
FD91-2	124064.62	278490.2	40764.59	1413741	436314	23415.8433	46831.6867
FO91-1	125524.08	333083.9	114102.8	4963240	755139.9	93464.0667	186928.133
FO91-2	140833.34	295074.1	104381.9	4575881	754293.2	100804.447	201608.893
FP91-1	117204.84	498348.2	135110.8	4420318	773736.4	91727.2267	183454.453
FP91-2	137110.96	402832.2	113162.1	4534410	809501.4	90726.2367	181452.473
FT91-1	155757.74	237463.3	48497.94	2994766	438569.1	50083.1433	100166.287
FT91-2	139966.26	166863.4	31690.15	2155341	306694.9	29107.5133	58215.0267

Relative atomic concentration corrected by inelastic mean free path and Scofield's relative sensitivity factor							
Electrolyte	Li 1s	C 1s	N 1s	O 1s	F 1s	S 2p (1/2)	S 2p (3/2)
F100-1	45918.72	10474.87	3651.259	50515.31	6501.056	8550.574	8735.4513
F100-2	56697.5	11960.08	2970.271	39259.11	5481.927	7349.158	7508.0589
FB91-1	58450.62	16811.69	2221.24	50228.71	6532.883	5270.491	5384.4471
FB91-2	48833.1	10355.96	1093.431	23797.29	3394.97	2805.873	2866.5407
FC91-1	55595.86	11419	2179.573	42326.88	5492.818	5374.553	5490.7594
FC91-2	47777.17	8434.285	721.325	17392.19	2021.805	1469.179	1500.9447
FD91-1	53183.01	14098.63	623.8453	28166.1	6788.513	1335.201	1364.0704
FD91-2	47690.75	8439.097	775.582	18071.37	4282.206	1381.197	1411.0605
FO91-1	48251.77	10093.45	2170.905	63443.39	7411.325	5513.031	5632.2316
FO91-2	54136.69	8941.64	1985.957	58491.92	7403.015	5946.007	6074.5697
FP91-1	45053.83	15101.46	2570.602	56503.41	7593.84	5410.582	5527.568
FP91-2	52705.79	12207.04	2153.008	57961.8	7944.856	5351.538	5467.2474
FT91-1	59873.66	7195.858	922.7158	38281.07	4304.339	2954.183	3018.0568
FT91-2	53803.38	5056.467	602.9328	27550.98	3010.058	1716.923	1754.0458

Relative atomic content ratio between bonding states based on deconvoluted XPS spectra for each element

C 1s	Relative atomic content ratio		
	C=O	C–O	C–C
F100	~ 0	0.291	0.709
FB91	~ 0	0.226	0.774
FC91	~ 0	0.214	0.786
FD91	0.090	0.225	0.686
FO91	~ 0	0.347	0.653
FP91	~ 0	0.275	0.725
FT91	~ 0	0.298	0.702

O 1s	Relative atomic content ratio		
	SO _x / C–O	C=O	Li ₂ O
F100	0.563	~ 0	0.437
FB91	0.467	~ 0	0.532
FC91	0.403	~ 0	0.597
FD91	0.372	0.084	0.544
FO91	0.759	~ 0	0.241
FP91	0.828	~ 0	0.172
FT91	0.599	~ 0	0.401

S 2p	Relative atomic content ratio	
	SO _x	Li ₂ S
F100	0.488	0.512
FB91	0.510	0.490
FC91	0.499	0.501
FD91	0.380	0.620
FO91	0.638	0.362
FP91	0.743	0.257
FT91	0.414	0.586

Supplementary Table 2. Calculated atomic contents (%) for each bonding state from each element taken from XPS spectra collected from SEI on Li metal cycled in Li|Li symmetric cells.

Assignment of atomic content of sulfur and oxygen to specific binding state is done by calculating the ratio of area under XPS spectra for each binding states. Atomic content of lithium tied to Li₂S, LiF, and Li₂O is estimated by stoichiometrically considering sulfur, fluorine, and oxygen content tied to the same binding state.

Element	Li 1s				C 1s				N 1s	O 1s			F 1s	S 2p	
	Li ₂ S	LiF	Li ₂ O	Li-X	C-F	C=O	C-O	C-C		SO _x / C-O	C=O	Li ₂ O		SO _x	Li ₂ S
F100	12.37	4.51	29.49	-7.68	~ 0	~ 0	2.46	5.99	2.49	19.02	~ 0	14.74	4.51	5.91	6.19
FB91	6.58	4.08	32.07	3.66	~ 0	~ 0	2.56	8.80	1.35	14.07	~ 0	16.03	4.08	3.43	3.29
FC91	6.14	3.42	32.83	9.47	~ 0	~ 0	2.09	7.69	1.31	11.10	~ 0	16.41	3.42	3.05	3.07
FD91	3.69	5.82	26.48	18.26	~ 0	1.06	2.65	8.11	0.77	9.07	2.04	13.24	5.82	1.13	1.85
FO91	5.87	5.19	20.58	4.22	~ 0	~ 0	2.32	4.35	1.46	32.42	~ 0	10.29	5.19	5.18	2.94
FP91	3.98	5.52	13.95	11.23	~ 0	~ 0	2.68	7.05	1.68	33.69	~ 0	6.98	5.52	5.74	1.99
FT91	5.18	3.46	24.99	20.83	~ 0	~ 0	1.73	4.06	0.72	18.66	~ 0	12.50	3.46	1.83	2.59

Supplementary Table 3. Formulation of reference electrolytes

Electrolyte Identifier	Formulation
Reference Electrolyte 1 (RE1)	1.0 M LiFSI in DME/TFEO (1.2:3 in mol%) ¹
Reference Electrolyte 2 (RE2)	1.2 M LiFSI in DMC/BTFE (1:2 in mol%) ²
Reference Electrolyte 3 (RE3)	LiFSI:DME:BTFE with the mole ratio of 1.0 : 2.0 : 1.2
Reference Electrolyte 4 (RE4)	LiFSI:DMC:TTE with the mole ratio of 1.0 : 2.0 : 1.2
Reference Electrolyte 5 (RE5)	1.0 M LiDFOB + 0.2 M LiBF ₄ in FEC/DEC (1:2 in vol%) ³
Reference Electrolyte 6 (RE6)	2.0 M LiTFSI + 2.0 M LiDFOB in DME ⁴
Reference Electrolyte 7 (RE7)	1.0 M LiPF ₆ in EC/DMC (50:50 vol%) with 10 wt% FEC

Supplementary Table 4. Raw data based on XPS survey scan collected from CEI on NMC811 cathode cycled in Li|NMC811 cells

Integrated peak intensity from XPS survey scan								
Element	Li 1s	C 1s	N 1s	O 1s	F 1s	S 2p (total)	S 2p (1/2)	S 2p (3/2)
F100-1	49884.53	1112382	158573.8	1640127	2603284.89	308050.47	102683.49	205366.98
F100-2	55605.44	1126649	177216.5	1706328	2587154.06	366689.3	122229.767	244459.533
FC91-1	31295.17	1464946	208371.5	1589001	3051750.44	476292.62	158764.207	317528.413
FC91-2	37856.45	1517250	202784.6	1408005	3045311.3	397312.87	132437.623	264875.247
FD91-1	13837.63	1689205	168431.3	1473341	2909944.77	375328.67	125109.557	250219.113
FD91-2	12753.78	1834613	142892.9	1303677	2960600.2	285175.79	95058.5967	190117.193

Relative atomic concentration corrected by inelastic mean free path and Scofield's relative sensitivity factor							
Element	Li 1s	C 1s	N 1s	O 1s	F 1s	S 2p (1/2)	S 2p (3/2)
F100-1	19175.74	33708.55091	3017.005708	20965.17	25549.95476	6056.844	6187.8026
F100-2	21374.87	34140.86939	3371.69863	21811.4	25391.63863	7209.792	7365.6794
FC91-1	12029.94	44392.30879	3964.449391	20311.66	29951.42251	9364.797	9567.2787
FC91-2	14552.11	45977.28455	3858.153729	17998.04	29888.22554	7811.908	7980.8143
FD91-1	5319.219	51188.02939	3204.552702	18833.21	28559.66994	7379.658	7539.2182
FD91-2	4902.585	55594.32091	2718.662861	16664.46	29056.82795	5607.085	5728.3194

Relative atomic content ratio between bonding states based on deconvoluted XPS spectra for each element

C 1s	Relative atomic content ratio					
	C–F ₂	O–C=O	C=O	C–O	C–C (F ₂ C–CF ₂)	C–C
F100	0.162	0.062	0.035	0.429	0.043	0.269
FC91	0.213	0.085	0.101	0.357	0.203	0.040
FD91	0.262	0.070	0.039	0.384	0.206	0.039

O 1s	Relative atomic content ratio	
	SO _x	M–O (Lattice O)
F100	0.896	0.104
FC91	1	~ 0
FD91	0.955	0.045

F 1s	Relative atomic content ratio	
	C–F	LiF
F100	0.379	0.621
FC91	0.742	0.258
FD91	0.952	0.048

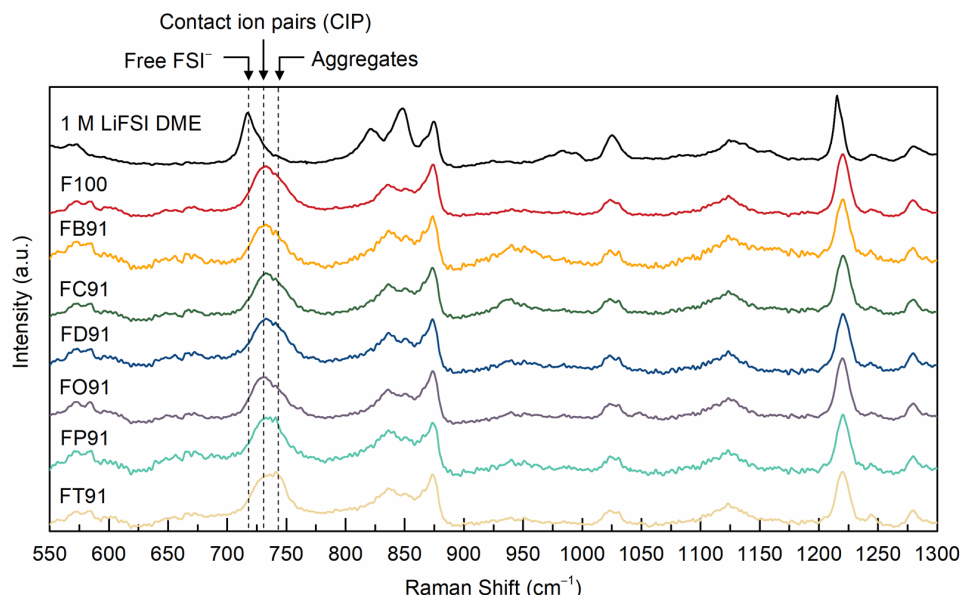
S 2p	Relative atomic content ratio	
	SO ₂	SO ₃
F100	0.746	0.254
FC91	1	0
FD91	1	0

Supplementary Table 5. Calculated atomic contents (%) for each bonding state from each element taken from XPS spectra collected from CEI on NMC811 cathode cycled in Li|NMC811 full cells.

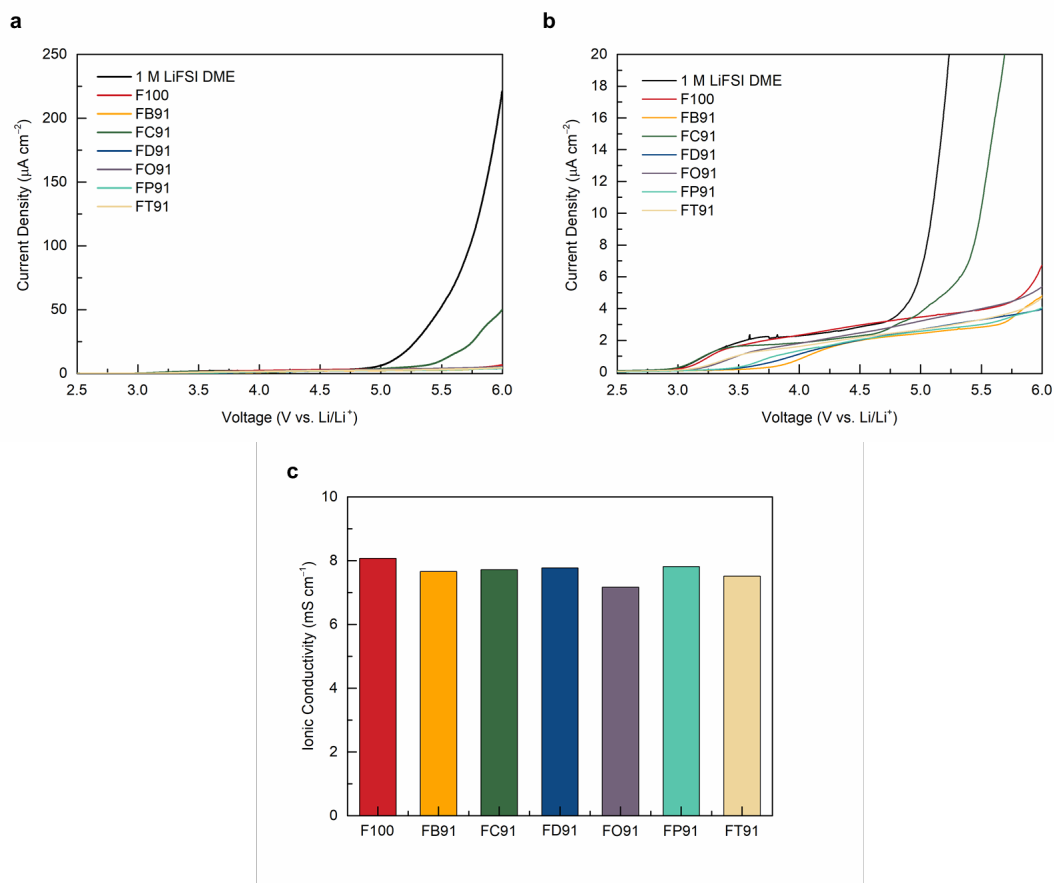
Assignment of atomic content of fluorine and oxygen to specific binding state is done by calculating the ratio of area under XPS spectra for each binding states. Atomic content of lithium tied to LiF is estimated by stoichiometrically considering fluorine, and oxygen content tied to the same binding state.

Element	Li 1s		C 1s					N 1s	O 1s	F 1s		S 2p		
	Binding State	LiF	Li-X	C-F ₂	O-C=O	C=O	C-O	C-C (F ₂ C-CF ₂)	C-C	N-SO _x	SO _x	C-F	LiF	SO ₂
F100	13.46	3.76	4.67	1.79	1.01	12.37	1.23	7.77	2.71	16.30	8.21	13.46	8.49	2.89
FC91	5.99	4.33	7.47	2.99	3.54	12.54	7.14	1.40	3.04	14.86	17.24	5.99	13.47	~ 0
FD91	1.13	3.09	11.55	3.07	1.73	16.92	9.09	1.73	2.44	13.99	22.65	1.13	10.83	~ 0

Supplementary Figures

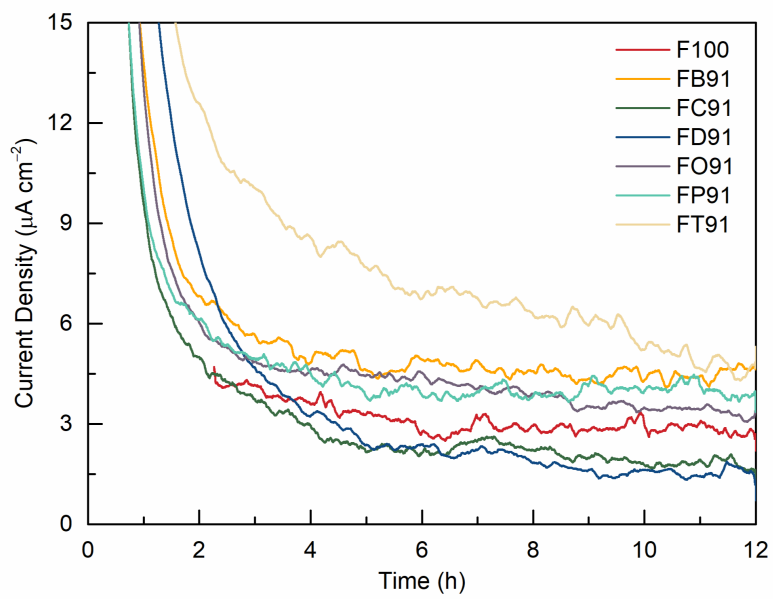


Supplementary Figure 1. Raman spectra differentiating the local solvation structure of dilute and locally super-concentrated electrolytes. A dilute electrolyte comprising 1.0 LiFSI in DME exhibits features in the Raman spectrum at 717 cm⁻¹ tied to S-N-S bending that are characteristic of fully dissolved (i.e., “free”) ions. In contrast, localized super-concentrated electrolytes featuring LiFSI as the salt, DME as the solvent, TTE as the diluent (F100) in a molar ratio of LiFSI:DME:TTE of 1 : 2 : 1.2 exhibit peaks at 730 cm⁻¹, and 746 cm⁻¹, characteristic of contact ion pairs and clustered ionic aggregates, respectively. Spectral signatures of mixed-anion localized super-concentrated electrolytes featuring LiFSI in combination with either LiBF₄ (FB91), LiClO₄ (FC91), LiDFOB (FD91), LiOTf (FO91), LiPF₆ (FP91), or LiTFSI (FT91) in a molar ratio of LiFSI:Salt:DME:TTE of 0.9 : 0.1 : 2 : 1.2 are similar to those in the absence of the second salt.

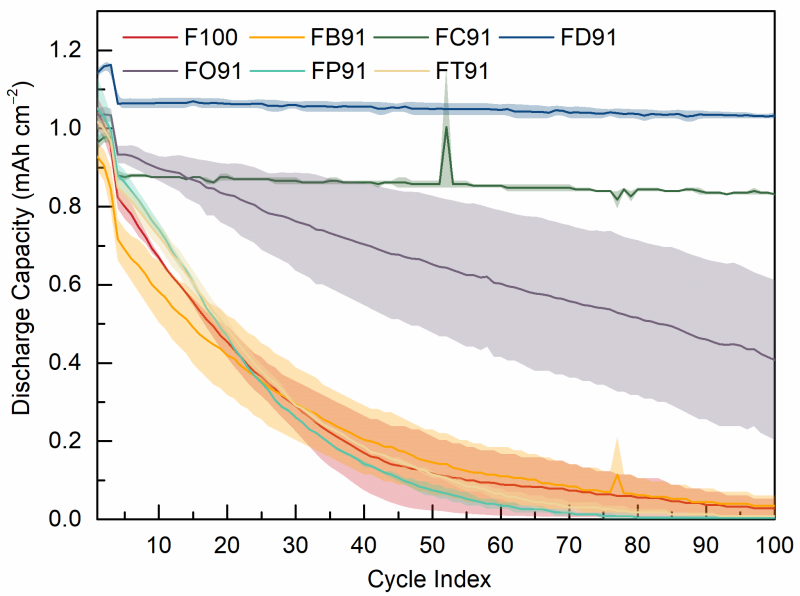


Supplementary Figure 2. Physical properties of dilute and locally super-concentrated electrolytes.

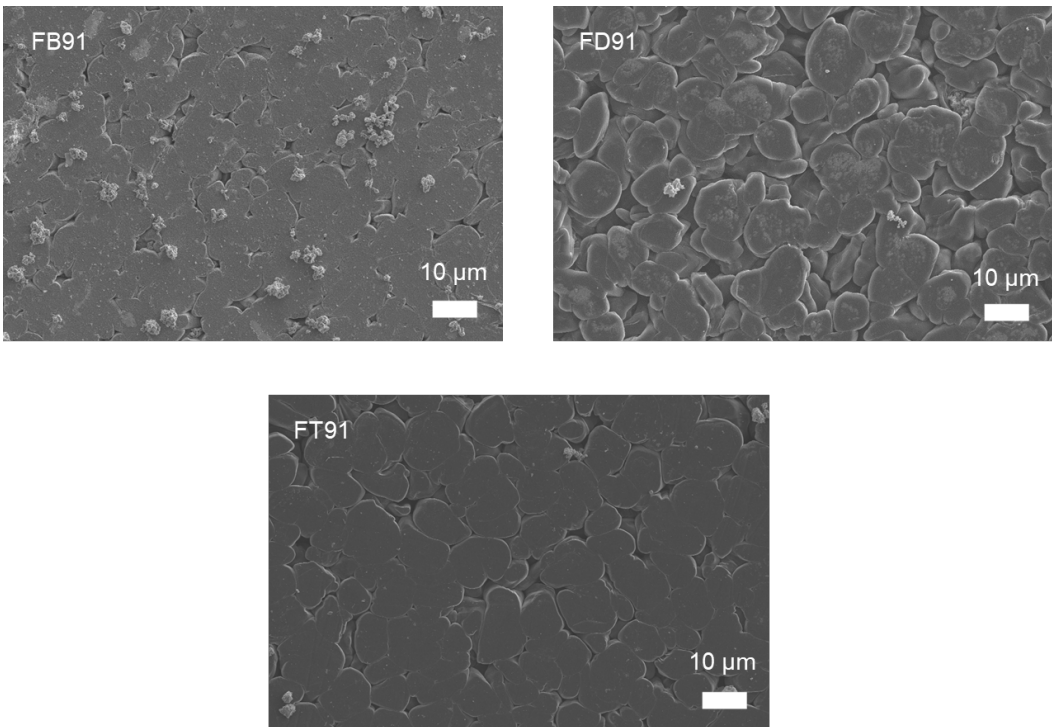
a, Ionic conductivity determined at 22.7–23.2 °C. **b** and **c**, Linear sweep voltammetry of electrolytes.



Supplementary Figure 3. Chronoamperometry for Li|NMC811 cells held at a constant voltage of 4.2 V. Leakage current density is lowest for mixed-anion locally super-concentrated electrolytes featuring LiFSI alongside either LiClO₄ or LiDFOB.

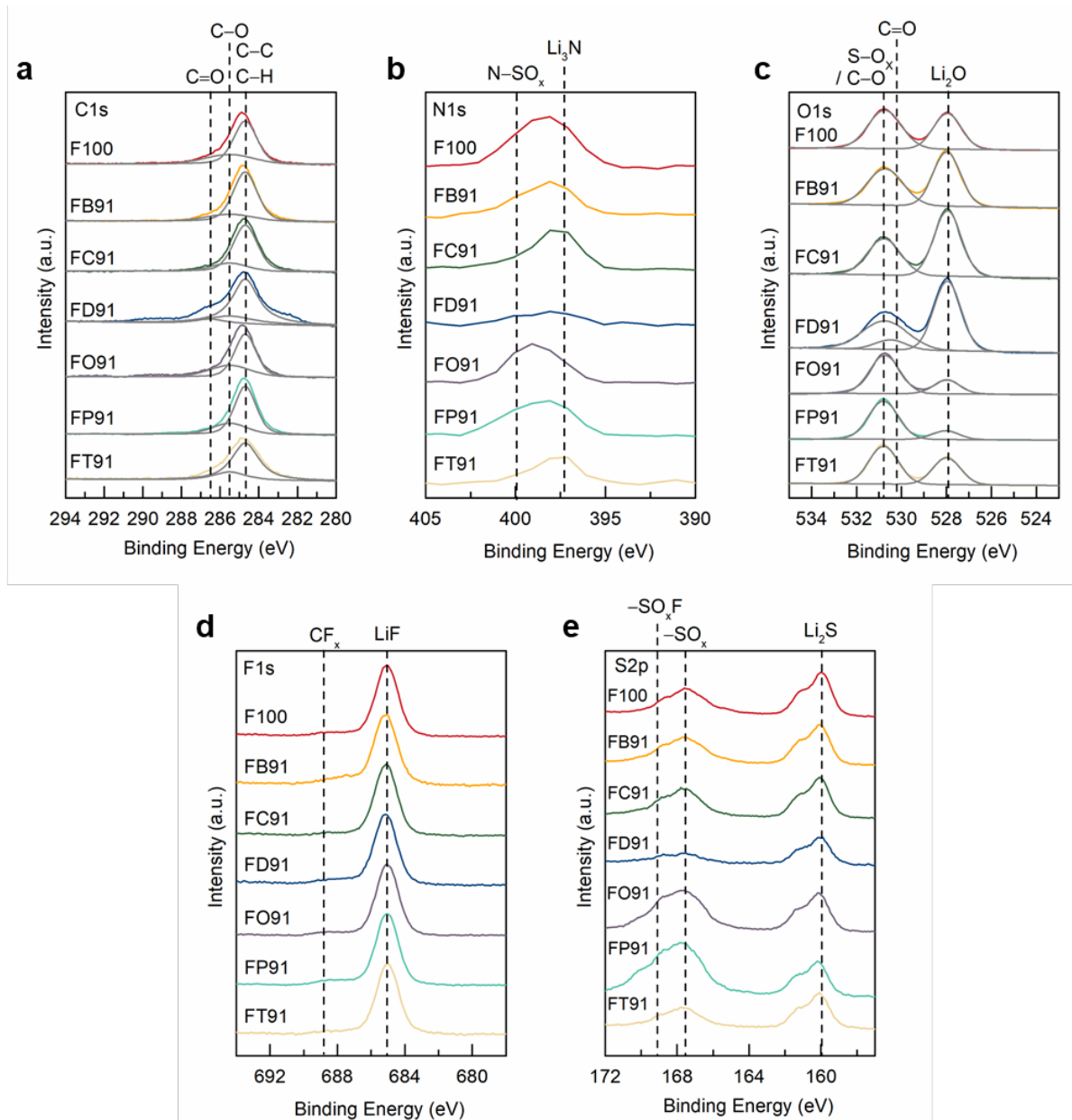


Supplementary Figure 4. Capacity retention of NMC|NMC symmetric cells cycled with single anion and mixed-anion LSCEs. FC91 and FD91 showed high capacity retention while others caused rapid capacity fade.

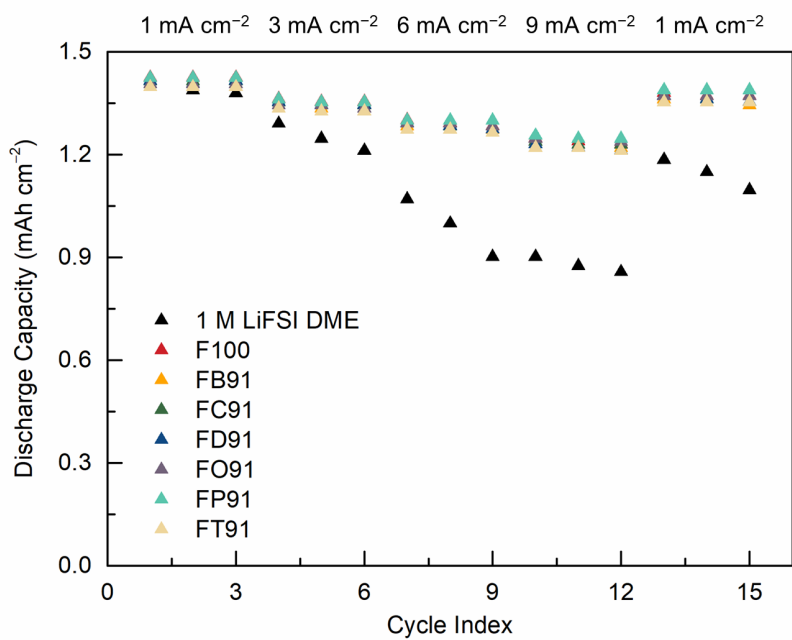


Supplementary Figure 5. Visualization of electrolyte-coupled lithium metal plating morphology.

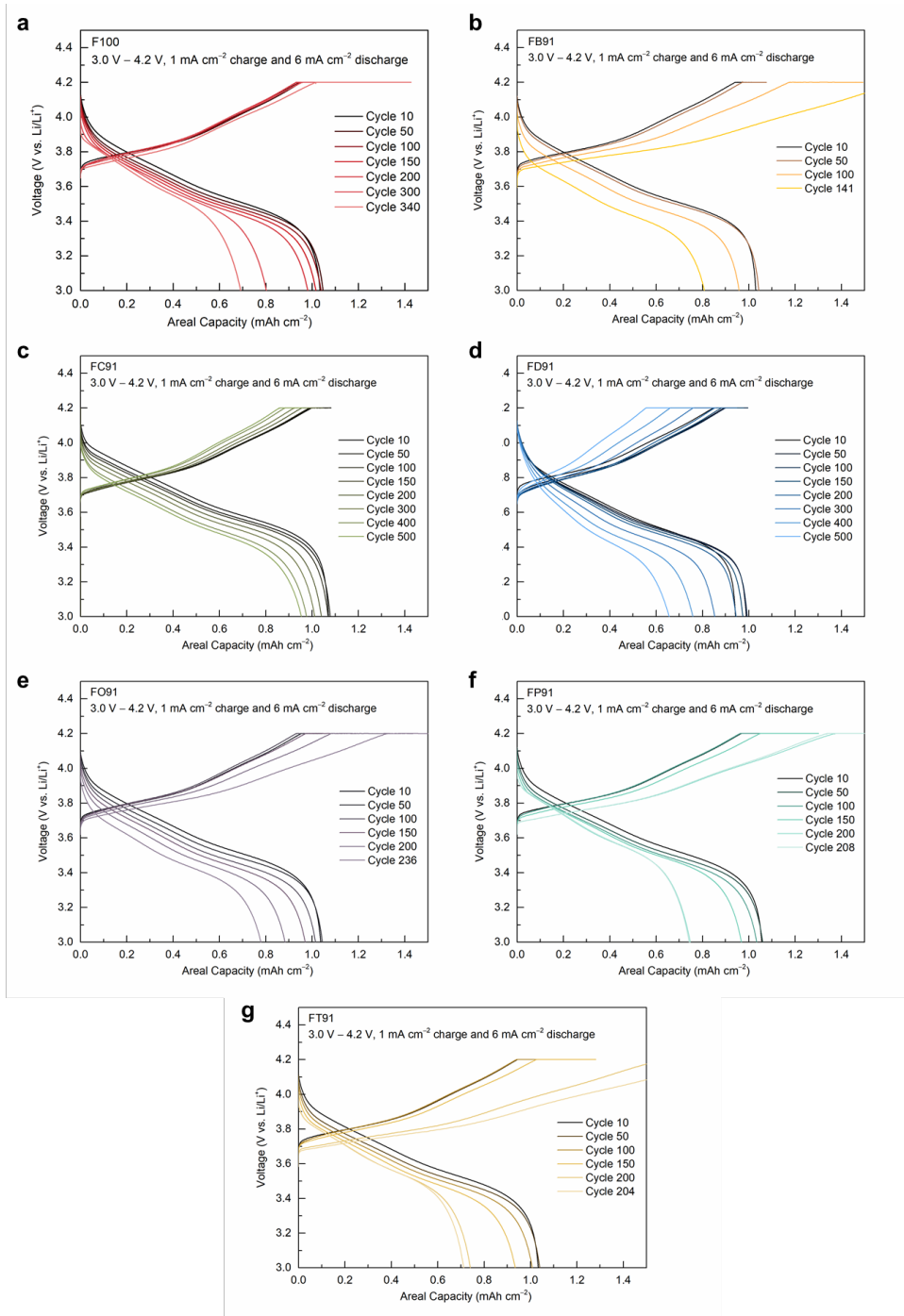
SEM images of the Li metal surface after 10 cycles of plating and stripping with locally super-concentrated electrolytes FB91, FD91, and FT91. The morphologies evidenced are significantly more planar and dense when FB91 and FT91 are used.



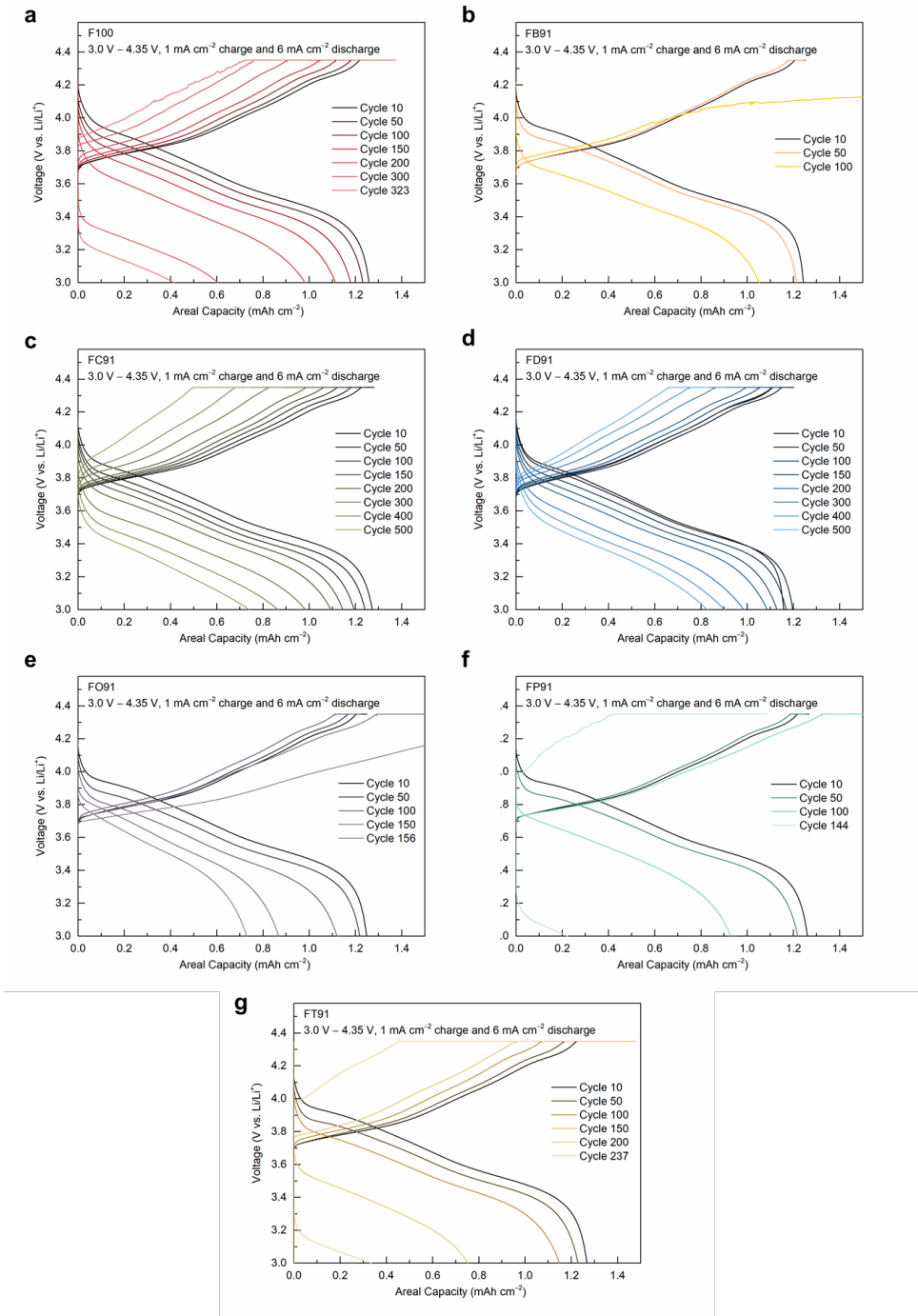
Supplementary Figure 6. X-ray photoelectroscopic analysis of Li anodes cycled with different electrolytes. **a**, C 1s spectra. **b**, N 1s spectra. **c**, O 1s spectra. **d**, F 1s spectra. **e**, S 2p spectra.



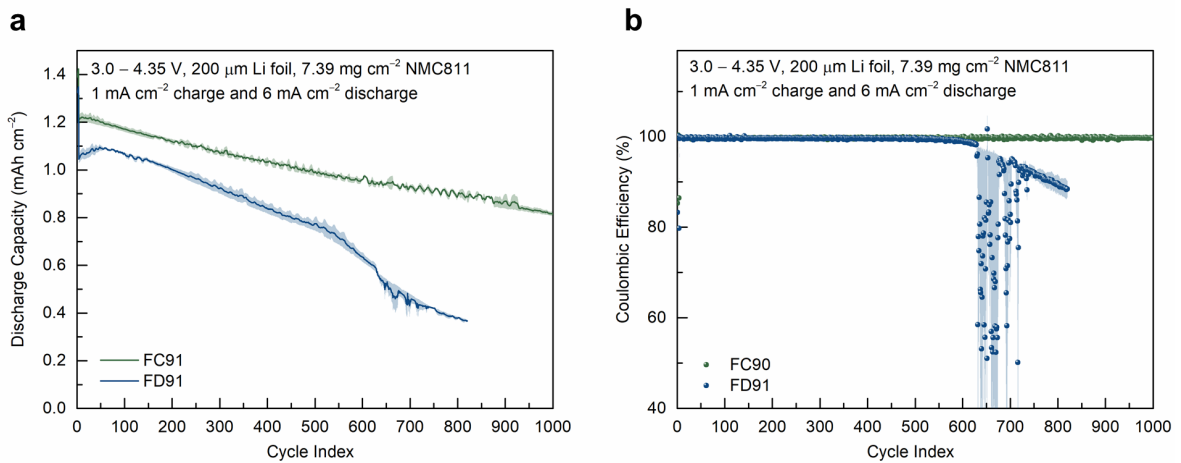
Supplementary Figure 7. Locally super-concentrated electrolytes with single-anion and mixed-anion chemistries outperform dilute electrolytes in rate tests. Rate capability of Li|NMC811 full cells. Cells were charged with a current density of 1 mA cm^{-2} and discharged with varying current densities as noted.



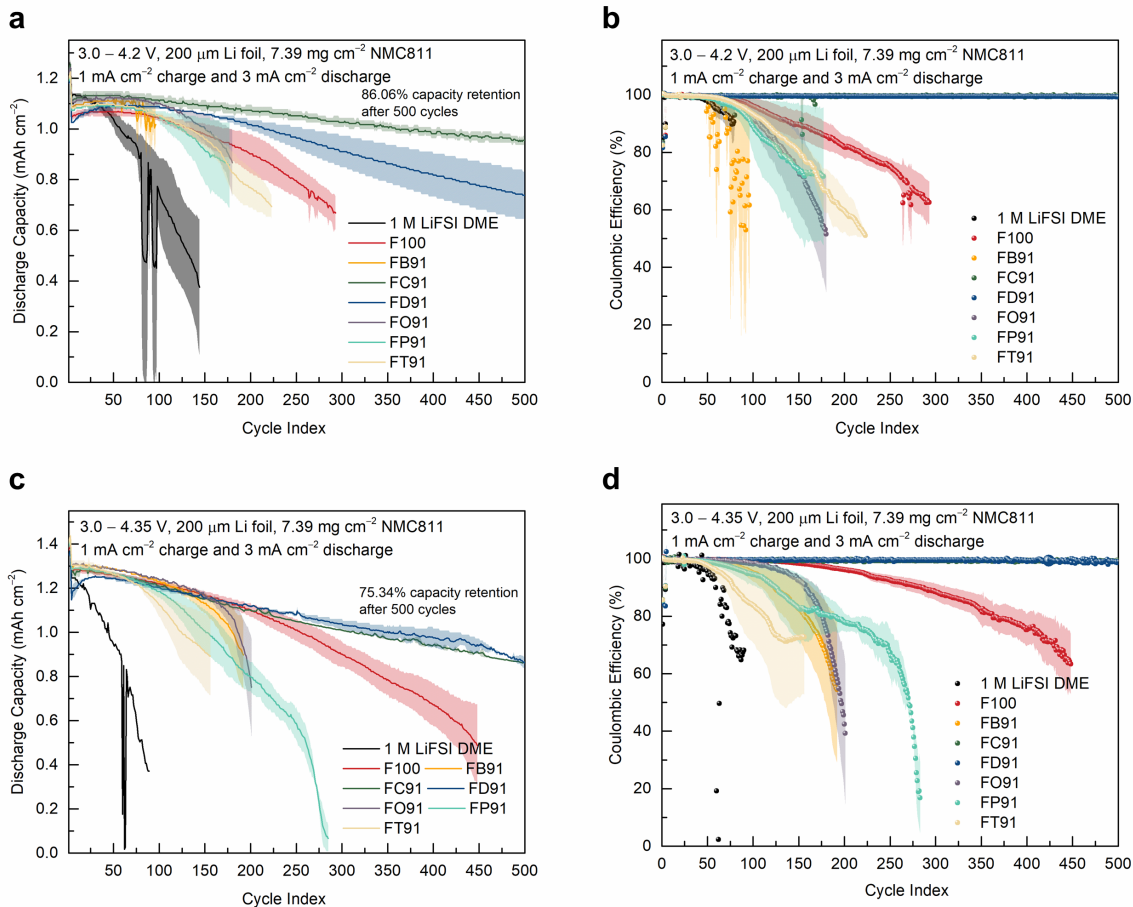
Supplementary Figure 8. Charge and discharge curves across the cycle life of Li|NMC811 cells charged to 4.2 V. Galvanostatic cycling profiles for Li|NMC811 cells charged at a current density of 1 mA cm^{-2} with a charge cut-off voltage of 4.2 V and discharged at a current density of 6 mA cm^{-2} with a discharge cut-off voltage of 3.0 V: **a**, F100; **b**, FB91; **c**, FC91; **d**, FD91; **e**, FO91; **f**, FP91; and **g**, FT91. At top of charge, a constant voltage-hold was implemented and sustained for 1 h, or until the current dropped below 0.1 mA cm^{-2} .



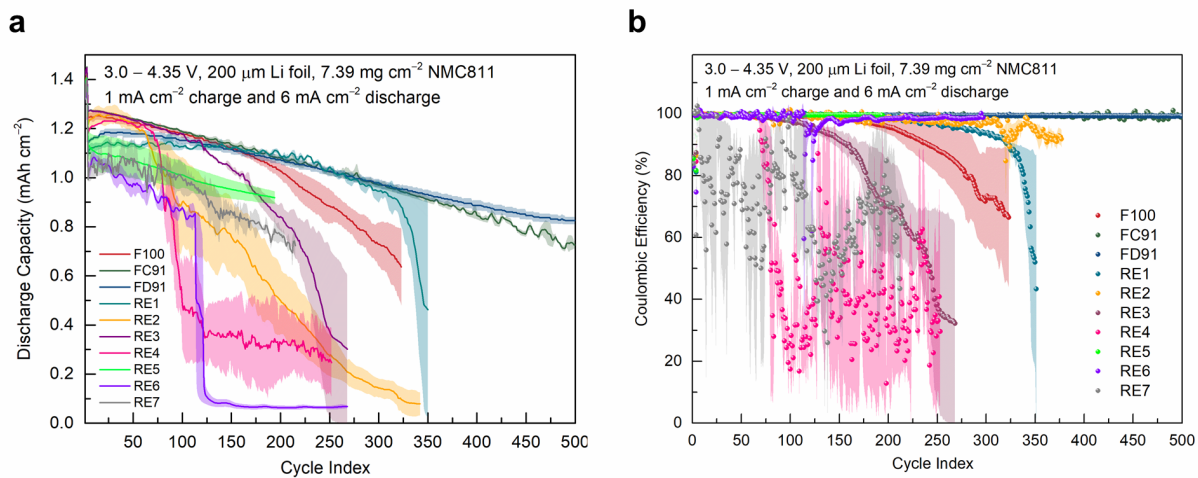
Supplementary Figure 9. Charge and discharge curves across the cycle life of Li|NMC811 cells charged to 4.35 V. Galvanostatic cycling profiles for Li|NMC811 cells charged at a current density of 1 mA cm⁻² with a charge cut-off voltage of 4.35 V and discharged at a current density of 6 mA cm⁻² with a discharge cut-off voltage of 3.0 V: **a**, F100; **b**, FB91; **c**, FC91; **d**, FD91; **e**, FO91; **f**, FP91; and **g**, FT91. At top of charge, a constant voltage-hold was implemented and sustained for 1 h, or until the current dropped below 0.1 mA cm⁻².



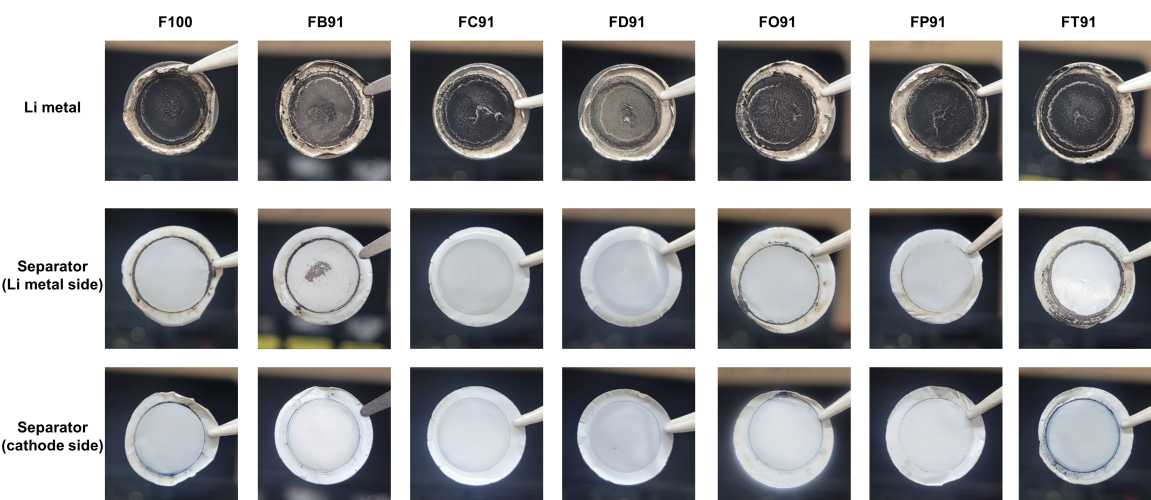
Supplementary Figure 10. Capacity retention and Coulombic efficiency for Li|NMC811 cells assembled with 200 μm -thick Li anodes under constant current charging protocol. **a**, Capacity retention of Li|NMC811 cells implementing FC91 and FD91 charged at a current density of 1 mA cm^{-2} with a charge cut-off voltage of 4.35 V and discharged at a current density of 6 mA cm^{-2} with a discharge cut-off voltage of 3.0 V. Cells were cycled without voltage holding step at 4.35 V during charging. The cells with FC91 showed ~70% capacity retention after 1000 cycles. **b**, Corresponding Coulombic efficiency.



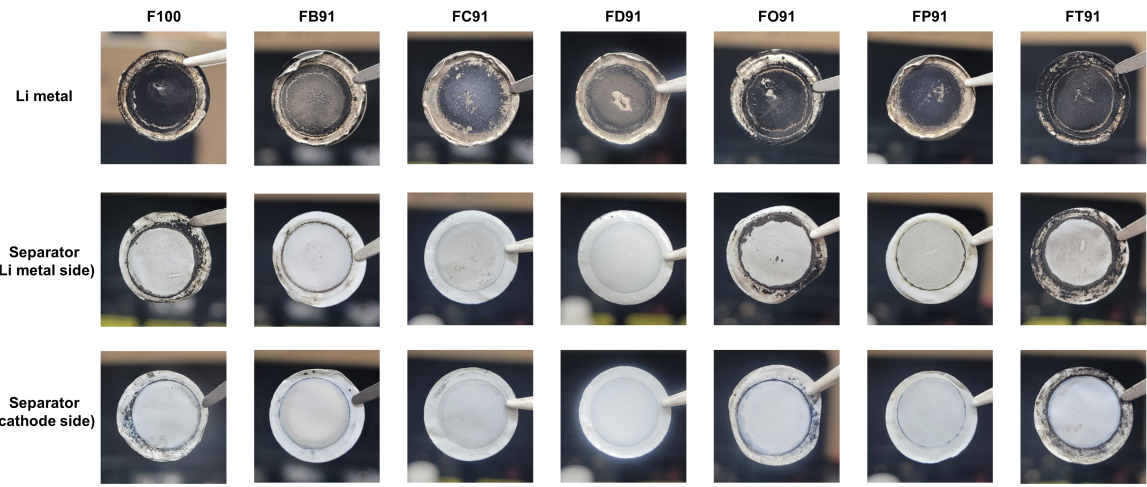
Supplementary Figure 11. Capacity retention and Coulombic efficiency for Li|NMC811 cells assembled with 200 μm -thick Li anodes. **a**, Capacity retention for Li|NMC811 cells charged at a current density of 1 mA cm^{-2} with a charge cut-off voltage of 4.2 V and discharged at a current density of 3 mA cm^{-2} with a discharge cut-off voltage of 3.0 V. **b**, Coulombic efficiency for Li|NMC811 cells charged at a current density of 1 mA cm^{-2} with a charge cut-off voltage of 4.2 V and discharged at a current density of 3 mA cm^{-2} with a discharge cut-off voltage of 3.0 V. **c**, Capacity retention for Li|NMC811 cells charged at a current density of 1 mA cm^{-2} with a charge cut-off voltage of 4.35 V and discharged at a current density of 3 mA cm^{-2} with a discharge cut-off voltage of 3.0 V. **d**, Coulombic efficiency for Li|NMC811 cells charged at a current density of 1 mA cm^{-2} with a charge cut-off voltage of 4.35 V and discharged at a current density of 3 mA cm^{-2} with a discharge cut-off voltage of 3.0 V. Whereas the theoretical cathode areal capacity based on NMC811 mass loading and 4.2 V cut-off voltage on charge is \sim 1.2 mAh cm^{-2} , it is \sim 1.4 mAh cm^{-2} when the cut-off voltage is raised to 4.35 V.



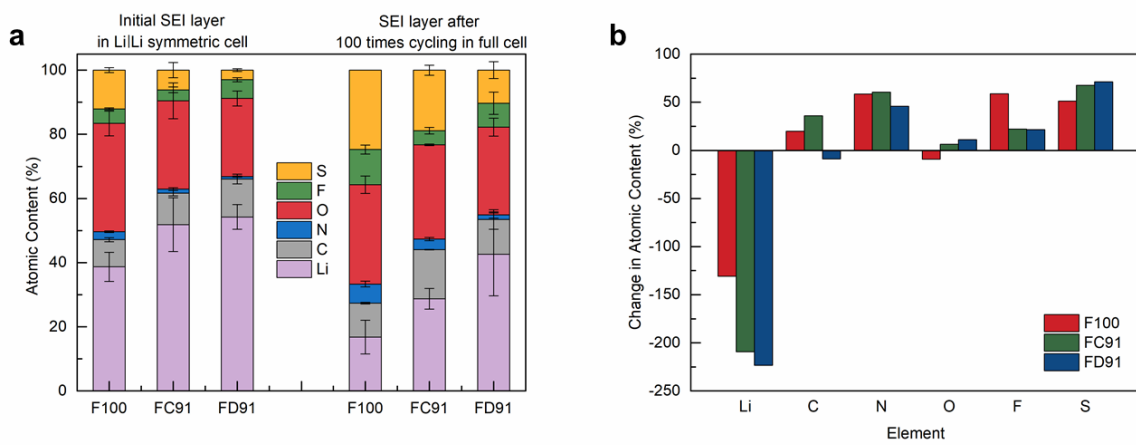
Supplementary Figure 12. Capacity retention and Coulombic efficiency for Li|NMC811 cells cycled with reference electrolytes. **a**, Capacity retention of Li|NMC811 cells using five reference electrolytes charged at a current density of 1 mA cm^{-2} with a charge cut-off voltage of 4.35 V and discharged at a current density of 6 mA cm^{-2} with a discharge cut-off voltage of 3.0 V. **b**, Coulombic efficiency of Li|NMC811 cells using five reference electrolytes charged at a current density of 1 mA cm^{-2} with a charge cut-off voltage of 4.35 V and discharged at a current density of 6 mA cm^{-2} with a discharge cut-off voltage of 3.0 V. Seven reference electrolytes are as follows; RE1 (1.0 M LiFSI in DME/TFEO (1.2:3 mol%)), RE2 (1.2 M LiFSI in DMC/BTFE (1:2 mol%)), RE3 (LiFSI:DME:BTFE with the mole ratio of 1.0 : 2.0 : 1.2), RE4 (LiFSI:DMC:TTE with the mole ratio of 1.0 : 2.0 : 1.2), RE5 (1.0 M LiDFOB + 0.2 M LiBF₄ in FEC/DEC (1:2 in vol%)), RE6 (2.0 M LiTFSI + 2.0 M LiDFOB in DME), and RE7 (1 M LiPF₆ in EC/DMC (50:50 vol%) with 10 wt% FEC). Data are presented as the mean and standard deviation of three independent trials.



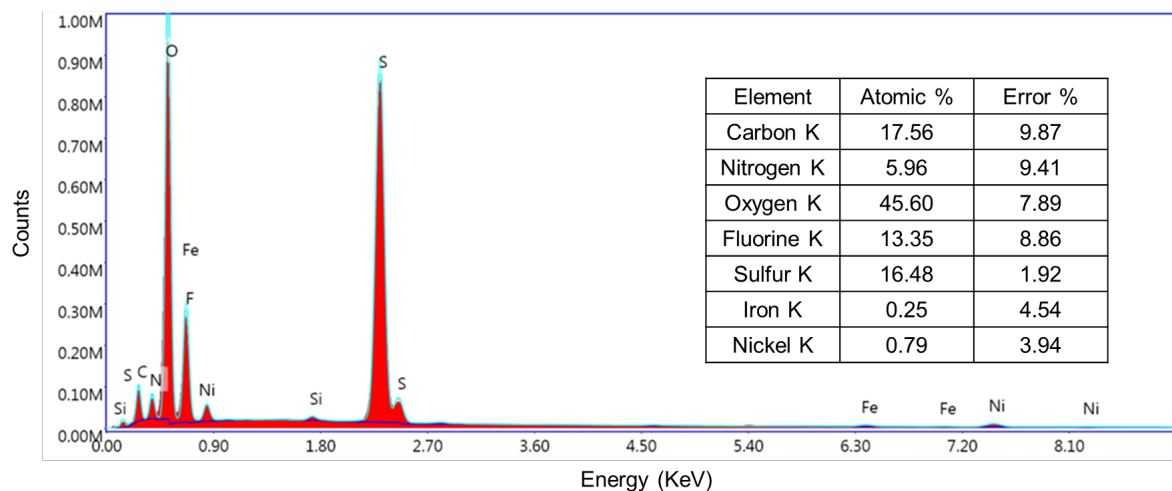
Supplementary Figure 13. Disassembly of Li|NMC811 cells reversibly charged to 4.2 V and discharged to 3.0 V after cycle 100. Images of cell components collected from Li|NMC811 cells cycled 100 times with locally super-concentrated electrolytes featuring single anion and mixed-anion chemistries. Li|NMC811 cells were charged at a current density of 1 mA cm^{-2} with a charge cut-off voltage of 4.2 V and discharged at a current density of 6 mA cm^{-2} with a discharge cut-off voltage of 3.0 V.



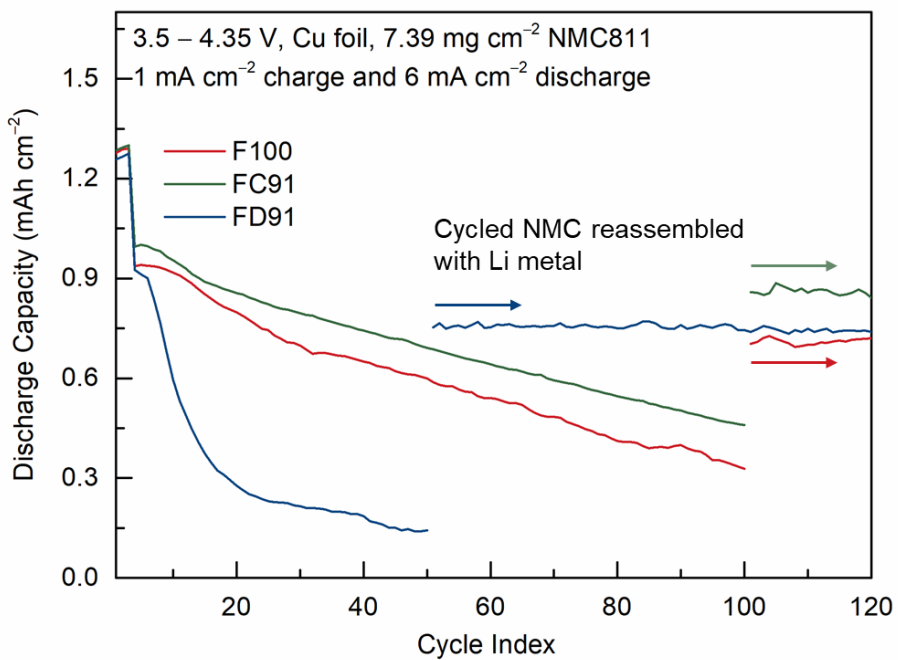
Supplementary Figure 14. Disassembly of Li|NMC811 cells reversibly charged to 4.35 V and discharged to 3.0 V after cycle 100. Images of cell components collected from Li|NMC811 cells cycled 100 times with locally super-concentrated electrolytes featuring single anion and mixed-anion chemistries. Li|NMC811 cells were charged at a current density of 1 mA cm^{-2} with a charge cut-off voltage of 4.35 V and discharged at a current density of 6 mA cm^{-2} with a discharge cut-off voltage of 3.0 V.



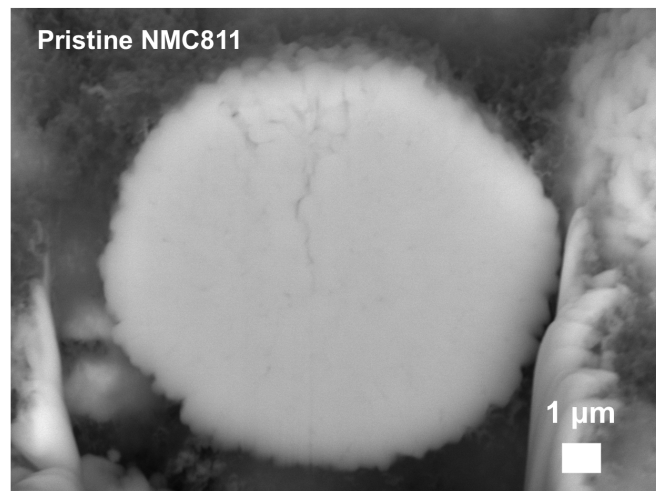
Supplementary Figure 15. XPS analysis of Li metal anodes in Li|Li and Li|NMC811 cells. **a**, Comparison of the SEI atomic make-up of the Li anode extracted from Li|Li cells and Li|NMC811 cells after cycle 100. **b**, Percent change in atomic content between the SEI formed on Li metal without and with contributing influence from the NMC811 cathode.



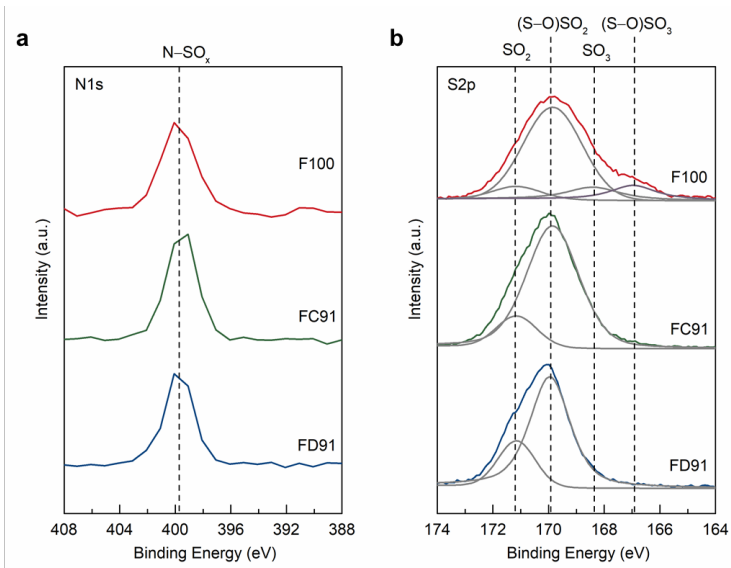
Supplementary Figure 16. SEM-EDX analysis data on Li metal cycled 250 times with F100 in Li|NMC811 cells. A notable characteristic of nickel are detected on the Li metal anode surface, confirming transition metal dissolution from the NMC811 cathode.



Supplementary Figure 17. Capacity retention of Cu|NMC811 cells cycled with F100, FC91 and FD91 and capacity retention of Li|NMC811 cells assembled with NMC cycled 50 times with FD91 and 100 times with F100 and FC91. Capacity recovery of Li|NMC811 cells rebuilt with cycled NMC implies that capacity retention of Cu|NMC811 cells is attributed to Li consumption at Cu anode.



Supplementary Figure 18. Microstructural characterization of NMC811 particles in composite cathodes. FIB-SEM cross-sectional analysis of a pristine composite NMC811 cathode, evidencing the polycrystallinity of NMC811 at the single-particle level.



Supplementary Figure 19. X-ray photoelectrochemical analysis on NMC811 cathode cycled in Li|NMC811 cells 100 times with charge cut-off voltage of 4.35 V and charge and discharge current density of 1 mA cm⁻² and 6 mA cm⁻², respectively. a, N 1s spectra. b, S 2p spectra.

Supplementary References

1. Cao, X. *et al.* Monolithic solid–electrolyte interphases formed in fluorinated orthoformate-based electrolytes minimize Li depletion and pulverization. *Nat. Energy* **4**, 796–805 (2019).
2. Chen, S. *et al.* High-voltage lithium-metal batteries enabled by localized high-concentration electrolytes. *Adv. Mater.* **30**, 1706102 (2018).
3. Weber, R. *et al.* Long cycle life and dendrite-free lithium morphology in anode-free lithium pouch cells enabled by a dual-salt liquid electrolyte. *Nat. Energy* **4**, 683–689 (2019).
4. Jiao, S. *et al.* Stable cycling of high-voltage lithium metal batteries in ether electrolytes. *Nat. Energy* **3**, 739–746 (2018).